Extended mean-field homogenization of unidirectional piezoelectric nanocomposites with generalized Gurtin-Murdoch interfaces

Qiang Chen, George Chatzigeorgiou*, Fodil Meraghni

Arts et Métiers Institute of Technology, CNRS, Université de Lorraine, LEM3-UMR7239, F-57000 Metz, France

Corresponding author: georges.chatzigeorgiou@ensam.eu

Abstract

This paper presents for the first time an extended Mori-Tanaka approach aimed at identifying the little-explored piezoelectric response of unidirectional nanoporous composites with energetic surfaces. The interface is simulated using the generalized Gurtin-Murdoch coherent interface model considering nonvanishing in-plane surface stress and surface electric displacement. The analytical solutions for Eshelby's inhomogeneity problems are obtained by solving four systems of equations, generated from the known macroscopic electromechanical loading conditions. The dilute concentration tensors for the fiber and energetic surface are evaluated exactly for coupled electromechanical fields, which are then utilized in the extended multiphysics Mori-Tanaka homogenization scheme. The reliability and accuracy of the extended theory are demonstrated through an extensive comparison with the predictions of the composite cylinder assemblage (CCA), the generalized self-consistent method (GSCM), as well as the finite-element (FE) homogenization technique. New results generated in this work demonstrate that, except for the transverse shear modulus, the extended Mori-Tanaka, CCA, and FE provide indistinguishable results under axisymmetric, axial shear, and electric loading, even at high volume fractions and small pore sizes where the surface piezoelectric effects are significant.

Keywords: Extended Mori-Tanaka Homogenization; Surface Piezoelectricity; Nanocomposites; Gurtin-Murdoch Interface; Electromechanical Loading

1. Introduction

The role of interface/surface in affecting the stiffness and strength of heterogeneous microstructures is well recognized. The interface can have an important contribution to not only the homogenized moduli but also the local stress field distribution, thereby impacting the plastic flow and failure modes [1-7]. In many cases, the assumption of the perfect interface in composite materials considering the inclusion and the matrix are well-bonded, cannot adequately describe the physical nature of the interface region. Therefore, different interface models have been developed according to their kinematic and kinetic characteristics [8-13], aiming at better identifying the underlying stress transfer mechanism across the interface region and eventually capturing the macroscopic behavior of the microstructures.

Surface stresses in solid bodies, which are the focus of the present work, are caused by the differences in configuration and in coordination numbers between atoms at the surface and in the bulk materials [14]. They are generally non-hydrostatic and non-homogeneous Moreover, in material processing, the surface of a material is frequently exposed to, e.g., oxidation, aging, grit blasting, plasma jet treatment, etc., thus possessing different properties from its adjacent bulk material [15]. In nanocomposite microstructures studied in this manuscript, the molecular dynamics simulations [16] reveal that the large surface-to-volume ratio could cause significant interfacial stress and energy along the surface that stretches between the inclusion and the matrix. A related feature of the nanostructures with surface stress and energy is the fact that the mechanical behaviors are size-dependent. More specifically, the local and homogenized responses of nanocomposites depend on the properties and curvature of the interface [17, 18]. The importance of surface stress and energy in nanocomposite structures has attracted considerable research attention over the past two decades through extensive atomistic simulations in the literature [19, 20]. From a continuum mechanics approach's point of view, surface stresses can be

phenomenologically interpreted as an elastic membrane equipped with its own potential energy. The surface elasticity model developed by Gurtin and Murdoch [21, 22] is widely accepted in the literature. The Gurtin-Murdoch interface model views the interface as an infinitesimally thin sheet between the inclusion and the matrix, characterized by its own elastic moduli. The interface is kinematically coherent, indicating the tangential strain components are equal to strains on the adjacent sides of the bulk materials.

The effect of surface stress and energy on the effective moduli and elastic fields of nanocomposites with the Gurtin-Murdoch interface has been extensively quantified through various micromechanics and homogenization approaches, defined by the representative volume element (RVE) concept for statistically homogeneous microstructures and the repeating unit cell (RUC) concept for periodic microstructures [23, 24]. Miller and Shenoy [25] obtained the surface elastic constants of single-crystal metals with two different crystallographic orientations using molecular dynamic simulations. Their contributions have spurred extensive use of the Gurtin-Murdoch interface model in the literature. For instance, employing the modified Mori-Tanaka approach, Duan and coworkers [26, 27] were perhaps the first to investigate systematically the homogenized elastic moduli of the nanoporous aluminum with the Gurtin-Murdoch interface model. Following this work, Chen et al. [28] developed the composite cylinder assemblage and the generalized self-consistent method with energetic surfaces. More recent contributions are the elasticity-based homogenization approaches such as the equivalent inhomogeneity method, Mogilevskaya et al. [29], the locally-exact homogenization theory, Wang et al. [30]. The finite-element, Javili et al. [31], Chatzigeorgiou et al. [8], Chen and Pindera [32], Kushch [19], and finite-volume-based, Chen et al. [32, 33], numerical homogenization theories are also favorable techniques due to their flexibility to handle more complicated microstructures and phase

constitutive laws. All the above studies indicate that depending on whether the surface energy is positive or negative, using the Gurtin-Murdoch interface model, nanoporous composites may produce either enhancement or reduction of the homogenized moduli when the pore radii are sufficiently small (typically below 20 nm), relative to materials with the same porosity volume fraction but much larger pore sizes. The readers are referred to the recent articles for more complete references in this area, cf. Wang et al. [34], Chen et al. [33], Firooz et al. [35], Mogilevskaya et al. [36].

Apart from the elastic behavior, there is a growing interest in developing micromechanics models for understanding the multiphysics response of piezoelectric/dielectric nanostructures due to their promising applications in nanoactuators and nanogenerators [37-41]. Such work has the potential to facilitate the efficient design and analysis of nano-sized functional components/devices. In piezoelectric nanostructures, in addition to surface stress, the surface energy can also depend on the surface electric displacement [42, 43]. Thus far, relatively few works have been devoted to incorporating surface piezoelectricity into the homogenization techniques albeit many micromechanics models are already available in the literature with multiphysics capabilities. An exception is a recent work by Chen et al. [44] who investigated in a systematical manner a full set of homogenized properties and local stress/electric fields of piezoelectric nanoporous composites with incorporated surface piezoelectricity for various pore radii and volume fractions using the multiphysics CCA/GSCM and finite-element as the gold solution. Prior to this study, Chen [45] developed the exact size-dependent connections between effective moduli of piezoelectric nanocomposites with interface effects using the generalized Hill's connections and Levin's formula. Xiao et al. [46] studied the effective electroelastic moduli of nanocomposites using the generalized self-consistent approach. Gu and Qin [47] established the bounds for the effective

properties of an inhomogeneous material with coherent imperfect interfaces in the setting of piezoelectricity using the classical minimum potential principles of linear piezoelectricity.

In this contribution, a generalized Mori-Tanaka method enhanced with surface piezoelectricity has been developed for the first time for identifying the homogenized moduli of unidirectional piezoelectric nanocomposites. The bulk material is transversely isotropic while the interface is modelled using the extended Gurtin-Murdoch model considering the in-plane surface stress and electric displacement. Kinematically coherent interface is considered wherein the mechanical displacement and electric potential continuity conditions hold between the fiber and matrix phase while the interfacial stress and electric displacement jump are governed by the surface equilibrium and electrostatic conditions, also known as the Young-Laplace equations [17]. Eshelby's inhomogeneity problems are solved analytically for four systems of equations, generated from the known macroscopic loading conditions, thereby permitting the exact computation of the dilute concentration piezoelectric tensors. The accuracy of the extended theory is validated extensively vis-à-vis the CCA/GSCM and finite-element predictions of Chen et al. [44].

The rest of the manuscript is organized as follows: Section 2 recalls the constitutive relation of the piezoelectric materials and introduces the generalized Gurtin-Murdoch coherent interface model. Sections 3 and 4 describe the generalized Eshelby's problem and Mori-Tanaka homogenization for inhomogeneity enhanced with energetic surfaces, respectively. Section 5 derives the analytical solutions for the determination of dilute concentration tensors for electromechanical fields under known macroscopic loading. Numerical results are generated in Section 6 to demonstrate the capabilities of the extended theory for accurate identification of the

homogenized moduli under various loading conditions. Section 7 draws pertinent conclusions. Useful equations for the analytical formalisms are provided in the Appendices.

2. Preliminaries

For a two-phase piezoelectric composite in which nano-inhomogeneities are randomly dispersed in the matrix phase, as shown in Figure 1, assuming small deformations/small rotations, electrostatic conditions with no electric charge, the strain tensor $\boldsymbol{\varepsilon}^{(q)}$ and the electric field vector $e^{(q)}$ in the qth phase in the Cartesian coordinates $\left(x_1, x_2, x_3\right)$ can be expressed with the help of the displacement vector $\mathbf{u}^{(q)}$ and the electric scalar potential $\phi^{(q)}$ respectively through the vector-type equations:

$$\boldsymbol{\varepsilon}^{(q)} = \frac{1}{2}\left(\nabla \mathbf{u}^{(q)} + \nabla \mathbf{u}^{\mathrm{T}(q)}\right), \qquad e^{(q)} = -\nabla \phi^{(q)} \tag{1}$$

where ∇ indicates the gradient operator. The superscripts $q = 0,1$ denote the matrix and fiber/porosity, respectively.

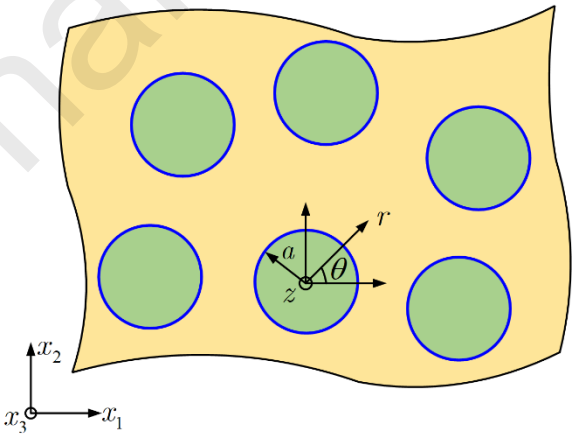

Figure 1 A piezoelectric solid with randomly-dispersed nano-fibers/porosities with a constant radius a. The Gurtin-Murdoch interface is highlighted in blue

On the other hand, the stress tensor and the electric displacement, written in vector-type forms, $\boldsymbol{\sigma}^{(q)}=\left[\sigma_{11},\sigma_{22},\sigma_{33},\sigma_{12},\sigma_{13},\sigma_{12}\right]^{(q)\mathrm{T}}$, $\boldsymbol{d}^{(q)}=\left[d_1,d_2,d_3\right]^{(q)\mathrm{T}}$, obey the equilibrium and the electrostatic equations:

$$\nabla\cdot\boldsymbol{\sigma}^{(q)}=0,\qquad \nabla\cdot\boldsymbol{d}^{(q)}=0 \tag{2}$$

where $\nabla\cdot$ represents the divergence operator.

A linear piezoelectric, transversely isotropic material obeys the following constitutive law, written in matrix-type notation:

$$\begin{aligned}\boldsymbol{\sigma}^{(q)}&=\mathbf{L}^{(q)}\cdot\boldsymbol{\varepsilon}^{(q)}-\mathbf{e}^{(q)}\cdot\mathbb{e}^{(q)}\\ \boldsymbol{d}^{(q)}&=\mathbf{e}^{(q)\mathrm{T}}\cdot\boldsymbol{\varepsilon}^{(q)}+\boldsymbol{\kappa}^{(q)}\cdot\mathbb{e}^{(q)}\end{aligned} \tag{3}$$

where $\mathbf{L}^{(q)}$, $\boldsymbol{\kappa}^{(q)}$ and $\mathbf{e}^{(q)}$ denote the 4th order elastic, 2nd order dielectric, and 3rd order piezoelectric tensors for the qth phase, respectively, whose matrix-type forms are given below for a transversely isotropic material:

$$\mathbf{L}^{(q)}=\begin{bmatrix}k+m & k-m & l & 0 & 0 & 0\\ k-m & k+m & l & 0 & 0 & 0\\ l & l & n & 0 & 0 & 0\\ 0 & 0 & 0 & m & 0 & 0\\ 0 & 0 & 0 & 0 & m & 0\\ 0 & 0 & 0 & 0 & 0 & p\end{bmatrix}^{(q)},\quad \mathbf{e}^{(q)}=\begin{bmatrix}0 & 0 & e_{31}\\ 0 & 0 & e_{31}\\ 0 & 0 & e_{33}\\ 0 & 0 & 0\\ e_{15} & 0 & 0\\ 0 & e_{15} & 0\end{bmatrix}^{(q)},\quad \boldsymbol{\kappa}^{(q)}=\begin{bmatrix}\kappa_{11} & 0 & 0\\ 0 & \kappa_{11} & 0\\ 0 & 0 & \kappa_{33}\end{bmatrix}^{(q)}$$

where k, l, n, m and p are Hill's moduli [48] for plane strain bulk modulus, cross modulus, unit uniaxial straining modulus, transverse shear modulus, and axial shear modulus, respectively. e_{31}, e_{33} and e_{15} are the non-zero piezoelectric constants. κ_{11} and κ_{33} are non-zero dielectric constants. In a compact form, Eq. (3) can be written as:

$$\sum^{(q)}=\mathcal{L}^{(q)}\cdot\mathbf{E}^{(q)} \tag{4}$$

where $\boldsymbol{\mathcal{L}}=\begin{bmatrix}\mathbf{L} & \mathbf{e}\\ \mathbf{e}^{\mathrm{T}} & -\boldsymbol{\kappa}\end{bmatrix}$ is the 9×9 symmetric matrix. $\sum=\left[\boldsymbol{\sigma},\boldsymbol{d}\right]^{\mathrm{T}}$ and $\mathbf{E}=\left[\boldsymbol{\varepsilon},-\mathbb{e}\right]^{\mathrm{T}}$ are the 12×1 vectors. Also, the generalized vector

$$\mathbf{U}^{(q)}=\left[u_1,u_2,u_3,\phi\right]^{(q)\mathrm{T}} \tag{5}$$

is introduced.

In addition to the bulk materials, it is assumed that an infinitesimally thin energetic interface between the fibers and the matrix can be modelled by the generalized Gurtin-Murdoch model [45]. For an energetic interface with a cylindrical shape of a constant radius a, the interface equations are better represented in cylindrical coordinates $\left(r,\theta,z\right)$. If the normal vector of the interface is parallel to the local axis r, the constitutive law of the surface reads:

$$\boldsymbol{\Sigma}^{(s)}=\boldsymbol{\mathcal{L}}^{(s)}\cdot\mathbf{E}^{(s)} \tag{6}$$

where the superscript s denotes an energetic surface and

$$\boldsymbol{\Sigma}^{(s)}=\begin{bmatrix}\sigma_{\theta\theta}\\ \sigma_{zz}\\ \sigma_{\theta z}\\ d_{\theta}\\ d_{z}\end{bmatrix}^{(s)},\quad \mathbf{E}^{(s)}=\begin{bmatrix}\varepsilon_{\theta\theta}\\ \varepsilon_{zz}\\ 2\varepsilon_{\theta z}\\ -\mathbb{e}_{\theta}\\ -\mathbb{e}_{z}\end{bmatrix}^{(s)},\quad \boldsymbol{\mathcal{L}}^{(s)}=\begin{bmatrix}L_{22} & L_{23} & 0 & 0 & e_{32}\\ L_{23} & L_{33} & 0 & 0 & e_{33}\\ 0 & 0 & L_{66} & e_{26} & 0\\ 0 & 0 & e_{26} & -\kappa_{22} & 0\\ e_{32} & e_{33} & 0 & 0 & -\kappa_{33}\end{bmatrix}^{(s)} \tag{7}$$

The interface is assumed to be kinematically coherent, indicating no atomic bonds are broken along the surface separating the two phases. The coherency of the surfaces can be interpreted as the tangential and axial components of the strain and electric field, in the cylindrical coordinates $\left(r,\theta,z\right)$, to be continuous across the interface as follows:

$$\begin{bmatrix} \varepsilon_{\theta\theta} \\ \varepsilon_{zz} \\ 2\varepsilon_{\theta z} \\ -e_{\theta} \\ -e_{z} \end{bmatrix}^{(s)} = \begin{bmatrix} \varepsilon_{\theta\theta}(a,\theta) \\ \varepsilon_{zz}(a,\theta,z) \\ 2\varepsilon_{\theta z}(a,\theta,z) \\ -e_{\theta}(a,\theta,z) \\ -e_{z}(a,\theta,z) \end{bmatrix}^{(0)} = \begin{bmatrix} \varepsilon_{\theta\theta}(a,\theta,z) \\ \varepsilon_{zz}(a,\theta,z) \\ 2\varepsilon_{\theta z}(a,\theta,z) \\ -e_{\theta}(a,\theta,z) \\ -e_{z}(a,\theta,z) \end{bmatrix}^{(1)} \tag{8}$$

The interface equilibrium and electrostatic equations are written as:

$$\begin{aligned} &-\frac{\sigma_{\theta\theta}^{(s)}}{a} + [\![\sigma_{rr}]\!] = 0 \\ &\frac{1}{a}\frac{\partial \sigma_{\theta\theta}^{(s)}}{\partial \theta} + \frac{\partial \sigma_{\theta z}^{(s)}}{\partial z} + [\![\sigma_{r\theta}]\!] = 0 \\ &\frac{1}{a}\frac{\partial \sigma_{\theta z}^{(s)}}{\partial \theta} + \frac{\partial \sigma_{zz}^{(s)}}{\partial z} + [\![\sigma_{rz}]\!] = 0 \\ &\frac{1}{a}\frac{\partial d_{\theta}^{(s)}}{\partial \theta} + \frac{\partial d_{z}^{(s)}}{\partial z} + [\![d_{r}]\!] = 0 \end{aligned} \tag{9}$$

where $[\![\{\bullet\}]\!] = \{\bullet\}^{+} - \{\bullet\}^{-} = \{\bullet\}^{(0)} - \{\bullet\}^{(1)}$. The displacement and electric potential continuity conditions are expressed through the relations

$$\begin{aligned} &u_i^{(1)}(a,\theta,z) = u_i^{(0)}(a,\theta,z), \quad i = r,\theta,z \\ &\phi^{(1)}(a,\theta,z) = \phi^{(0)}(a,\theta,z) \end{aligned} \tag{10}$$

3. Eshelby's problem for inhomogeneity with energetic interface

Identifying the overall properties of a composite sensitive to electromechanical loading conditions is the task of homogenization strategies and techniques. In this manuscript, the mean-field approach of the Mori-Tanaka method is followed. This method relies on two aspects: i) solving a basic (Eshelby-type) problem of an inhomogeneity embedded in an infinite medium, allowing to compute the so-called "dilute concentration" tensors, and ii) using this information at the level of the composite for identifying the "concentration" tensors, whose knowledge leads to link the

microscopic and macroscopic fields and to obtain the macroscopic matrix $\boldsymbol{\mathcal{L}}^{\#}$ of the overall composite.

Consider a cylindrical inhomogeneity, embedded in an infinite medium, as shown in Figure 2. The medium and the inhomogeneity are characterized by constant generalized moduli $\boldsymbol{\mathcal{L}}^{(0)}$ and $\boldsymbol{\mathcal{L}}^{(1)}$ respectively. The inhomogeneity occupies the space Ω_1 with volume V_1 and is bounded by the energetic interface $\mathcal{S}$ with the unit normal vector $\mathbf{n}$. The medium occupies the space Ω_0, which is extended to infinity (boundary surface Ω_∞). At far distance, a linear field

$$\mathbf{U}^{ext} = \begin{bmatrix} u_1^0 \\ u_2^0 \\ u_3^0 \\ \phi^0 \end{bmatrix} = \begin{bmatrix} \varepsilon_{11}^0 x_1 + \varepsilon_{12}^0 x_2 + \varepsilon_{13}^0 x_3 \\ \varepsilon_{12}^0 x_1 + \varepsilon_{22}^0 x_2 + \varepsilon_{23}^0 x_3 \\ \varepsilon_{13}^0 x_1 + \varepsilon_{23}^0 x_2 + \varepsilon_{33}^0 x_3 \\ -e_1^0 x_1 - e_2^0 x_2 - e_3^0 x_3 \end{bmatrix} \tag{11}$$

with ε_{ij}^0 , e_i^0 $\left(i, j = 1,2,3\right)$ constant values applied.

For this problem, which is a generalized version of the famous Eshelby inhomogeneity problem [49] accounting for multiphysics phenomena, the constitutive law is position-dependent and reads

$$\boldsymbol{\Sigma}(\boldsymbol{x}) = \begin{cases} \boldsymbol{\mathcal{L}}^{(0)} \cdot \mathbf{E}(\boldsymbol{x}), & \boldsymbol{x} \in \Omega_0 \\ \boldsymbol{\mathcal{L}}^{(1)} \cdot \mathbf{E}(\boldsymbol{x}), & \boldsymbol{x} \in \Omega_1 \end{cases} \tag{12}$$

The boundary conditions correspond to uniform $\mathbf{E}^{(0)}$ at a far distance.

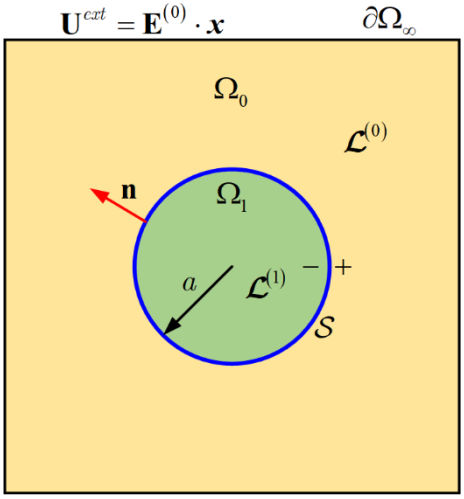

Figure 2 Cross section of cylindrical fiber with the energetic interface (highlighted in blue) inside an infinite medium. The medium is subjected to linear displacement and electric potential at a far distance

For the pure mechanical problem, Gu et al. [50], based on the methodology of Duan et al. [51], proposed to substitute the inhomogeneity/interface system with an equivalent particle, using energy principles. Instead of that, we propose to identify dilute concentration tensors according to the formulas:

$$\langle \mathbf{E} \rangle_{\Omega_1}^{+} = \mathbf{T} \cdot \mathbf{E}^{(0)}, \qquad \langle \boldsymbol{\Sigma} \rangle_{\Omega_1}^{+} = \mathbf{H} \cdot \mathbf{E}^{(0)} \tag{13}$$

with

$$\langle \mathbf{E} \rangle_{\Omega_1}^{+} = \frac{1}{|\Omega_1|} \int_{\mathcal{S}} \boldsymbol{\mathcal{N}}^{\mathrm{T}} \cdot \mathbf{U} \mathrm{d}S \tag{14}$$

$$\langle \boldsymbol{\Sigma} \rangle_{\Omega_1}^{+} = \frac{1}{|\Omega_1|} \int_{\Omega_1} \boldsymbol{\Sigma}^{-} \, \mathrm{d}V + \frac{1}{|\Omega_1|} \int_{\mathcal{S}} \boldsymbol{\Sigma}^{(s)} \, \mathrm{d}S \tag{15}$$

and

$$\boldsymbol{\mathcal{N}} = \begin{bmatrix} n_1 & 0 & 0 & n_2 & n_3 & 0 & 0 & 0 & 0 \\ 0 & n_2 & 0 & n_1 & 0 & n_3 & 0 & 0 & 0 \\ 0 & 0 & n_3 & 0 & n_1 & n_2 & 0 & 0 & 0 \\ 0 & 0 & 0 & 0 & 0 & 0 & n_1 & n_2 & n_3 \end{bmatrix} \tag{16}$$

where the superscripts "+" and "−" signs represent the fiber and matrix side of the interface, respectively. We note that while $\mathbf{T}$ represents the classical dilute strain concentration tensor, $\mathbf{H}$ differs from the definition of a classical dilute stress concentration tensor [52]. It is recalled that for an energetic interface, the continuity of displacement across the interface holds.

4. Mori-Tanaka method for composites with energetic interfaces

Consider now an RVE that occupies the space $\mathcal{B}$ with volume V. The boundary surface $\mathcal{B}$ is subjected to macroscopic $\overline{\mathbf{E}}$. The inhomogeneity occupies the space $\mathcal{B}_1$ with volume V_1 and the matrix occupies the space $\mathcal{B}_0$ with volume V_0. Obviously $\mathcal{B}=\mathcal{B}_1\cup\mathcal{B}_0$ and $V=V_1+V_0$. The inhomogeneity has a volume fraction $v_f=V_1/V$. According to the Mori-Tanaka theory, the macroscopic $\overline{\mathbf{E}}$ and $\overline{\boldsymbol{\Sigma}}$ tensors are related to the corresponding fields in the inhomogeneity and the interface according to the formulas

$$\begin{aligned}\overline{\mathbf{E}}&=\frac{1}{V}\int_{\mathcal{B}}\mathbf{E}\,\mathrm{d}V=\left[1-v_f\right]\mathbf{E}^{(0)}+v_f\mathbf{T}\cdot\mathbf{E}^{(0)},\\ \overline{\boldsymbol{\Sigma}}&=\frac{1}{V}\int_{\mathcal{B}}\boldsymbol{\Sigma}\,\mathrm{d}V+\frac{1}{V}\int_{\mathcal{S}}\boldsymbol{\Sigma}^{(s)}\,\mathrm{d}S=\left[1-v_f\right]\boldsymbol{\mathcal{L}}^{(0)}\cdot\mathbf{E}^{(0)}+v_f\mathbf{H}\cdot\mathbf{E}^{(0)}\end{aligned}\tag{17}$$

From these formulas one has

$$\begin{aligned}\mathbf{E}^{(0)}&=\left[\left[1-v_f\right]\boldsymbol{\mathcal{I}}+v_f\mathbf{T}\right]^{-1}\cdot\overline{\mathbf{E}}=\mathbf{A}_0\cdot\overline{\mathbf{E}},\\ \mathbf{E}^{(1)}&=\mathbf{T}\cdot\mathbf{A}_0\cdot\overline{\mathbf{E}}=\mathbf{A}_1\cdot\overline{\mathbf{E}},\\ \overline{\boldsymbol{\Sigma}}&=\left[\left[1-v_f\right]\boldsymbol{\mathcal{L}}^{(0)}+v_f\mathbf{H}\right]\cdot\mathbf{A}_0\cdot\overline{\mathbf{E}}=\boldsymbol{\mathcal{L}}^{*}\cdot\overline{\mathbf{E}}\end{aligned}\tag{18}$$

where $\boldsymbol{\mathcal{I}}$ denotes the fourth-order identity tensor. The dilute concentration tensors are obtained through the CCA method.

5. Analytical solutions for four special boundary-value problems

This approach is motivated by the studied boundary value problems by Hashin and Rosen [53] in their famous composite cylinders assemblage theory. The necessary modifications on these problems, discussed in the sequel, provide the exact solution for the dilute concentration tensors. Similar technique has been utilized in various articles for studying the mechanical and piezoelectric response of long fiber composites [54-57]. Before passing to the actual boundary value problems, it is essential to express all the fields and the conservation laws in cylindrical coordinates.

5.1 Expressing Eshelby's inhomogeneity problem in cylindrical coordinates

Inside the representative volume element, the various fields generated at every phase ($q = 0,1$) depend on the spatial position, i.e

$$\mathbf{U}^{(q)}(\boldsymbol{x}),\ \ \mathbf{E}^{(q)}(\boldsymbol{x}),\ \ \boldsymbol{\Sigma}^{(q)}(\boldsymbol{x}),\ \ \forall \boldsymbol{x} \in \Omega_q \tag{19}$$

Due to the geometry of the inhomogeneities, the problem can be transformed into cylindrical coordinates, using a system of concentric cylinders for the inhomogeneity and the infinite matrix, according to the equations in Appendix A. In cylindrical coordinates, the axes (x_1, x_2, x_3) are transformed to (r, θ, z), according to the relations

$$x_1 = r\cos\theta,\ \ x_2 = r\sin\theta,\ \ x_3 = z \tag{20}$$

The vectors $\mathbf{U}$, $\mathbf{E}$ and $\boldsymbol{\Sigma}$ in cylindrical coordinates are expressed as

$$\mathbf{U}^{(q)}=\begin{bmatrix}u_r\\u_\theta\\u_z\\\phi\end{bmatrix}^{(q)},\quad \mathbf{E}^{(q)}=\begin{bmatrix}\varepsilon_{rr}\\\varepsilon_{\theta\theta}\\\varepsilon_{zz}\\2\varepsilon_{r\theta}\\2\varepsilon_{rz}\\2\varepsilon_{\theta z}\\-e_r\\-e_\theta\\-e_z\end{bmatrix}^{(q)},\quad \mathbf{\Sigma}^{(q)}=\begin{bmatrix}\sigma_{rr}\\\sigma_{\theta\theta}\\\sigma_{zz}\\\sigma_{r\theta}\\\sigma_{rz}\\\sigma_{\theta z}\\d_r\\d_\theta\\d_z\end{bmatrix}^{(q)} \tag{21}$$

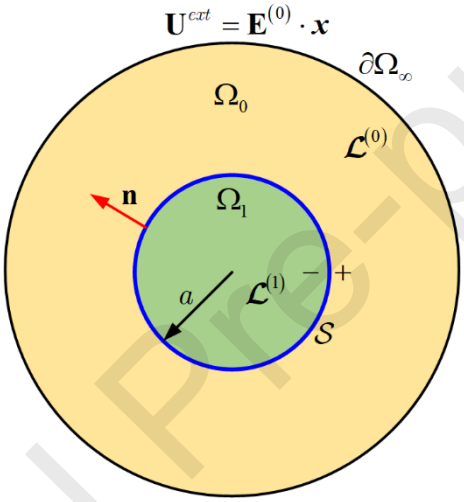

Figure 3 Cross section of cylindrical fiber with the energetic interface (highlighted in blue) inside an infinite medium. All the fields are expressed in cylindrical coordinates

In the cylindrical coordinate system, the equilibrium and electrostatic equations are written as

$$\begin{aligned}
&\frac{\partial\sigma_{rr}^{(q)}}{\partial r}+\frac{1}{r}\frac{\partial\sigma_{r\theta}^{(q)}}{\partial\theta}+\frac{\sigma_{rr}^{(q)}-\sigma_{\theta\theta}^{(q)}}{r}+\frac{\partial\sigma_{rz}^{(q)}}{\partial z}=0,\\
&\frac{\partial\sigma_{r\theta}^{(q)}}{\partial r}+\frac{1}{r}\frac{\partial\sigma_{\theta\theta}^{(q)}}{\partial\theta}+\frac{2\sigma_{r\theta}^{(q)}}{r}+\frac{\partial\sigma_{\theta z}^{(q)}}{\partial z}=0,\\
&\frac{\partial\sigma_{rz}^{(q)}}{\partial r}+\frac{1}{r}\frac{\partial\sigma_{\theta z}^{(q)}}{\partial\theta}+\frac{\sigma_{rz}^{(q)}}{r}+\frac{\partial\sigma_{zz}^{(q)}}{\partial z}=0,\\
&\frac{\partial d_r^{(q)}}{\partial r}+\frac{1}{r}\frac{\partial d_\theta^{(q)}}{\partial\theta}+\frac{d_r^{(q)}}{r}+\frac{\partial d_z^{(q)}}{\partial z}=0
\end{aligned} \tag{22}$$

while the $\mathbf{E}$ components at each phase are given by the expressions

$$\mathbf{E}^{(q)} = \begin{bmatrix} \partial u_r^{(q)} / \partial r \\ (1/r)\partial u_\theta^{(q)} / \partial \theta + u_r^{(q)} / r \\ \partial u_z^{(q)} / \partial z \\ \partial u_\theta^{(q)} / \partial r + (1/r)\partial u_r^{(q)} / \partial \theta - u_\theta^{(q)} / r \\ \partial u_z^{(q)} / \partial r + \partial u_r^{(q)} / \partial z \\ (1/r)\partial u_z^{(q)} / \partial \theta + + \partial u_\theta^{(q)} / \partial z \\ \partial \phi^{(q)} / \partial r \\ (1/r)\partial \phi^{(q)} / \partial \theta \\ \partial \phi^{(q)} / \partial z \end{bmatrix} \tag{23}$$

The inhomogeneity is considered to have a constant radius $r = a$.

Due to the transverse isotropy of all phases, the generalized stiffness matrix $\mathcal{L}$ retains the same form in cylindrical coordinates. In the following subsections, the boundary value problems are presented and the analytical form of the solutions (in terms of the generalized vector $\mathbf{U}^{(q)}$) is obtained.

5.2 Axial shear/in-plane electric field

Under this loading mode, displacement and electric potential boundary conditions at the far field ($r^{ext} \to \infty$) read:

$$\begin{aligned} u_r^{ext} &= u_\theta^{ext} = 0, \\ u_z^{ext} &= \beta r^{ext} \cos\theta, \\ \phi^{ext} &= -\beta^e r^{ext} \cos\theta \end{aligned} \tag{24}$$

where β and β^e are arbitrary known constants. The analytical solution for the displacement field and the electric potential at every r, θ and z takes the form

$$
\begin{aligned}
u_r^{(q)} &= u_\theta^{(q)} = 0, \\
u_z^{(q)} &= r\sum_{i=1}^{2} \Xi_{q,i} \left[\frac{r}{a}\right]^{\xi_i - 1} \cos\theta, \\
\phi^{(q)} &= -r\sum_{i=1}^{2} \Xi_{q,i}^{e} \left[\frac{r}{a}\right]^{\xi_i - 1} \cos\theta
\end{aligned}
\tag{25}
$$

with $\xi_1 = 1$ and $\xi_2 = -1$. The unknown coefficients $\Xi_{q,i}$ and $\Xi_{q,i}^{e}$ are determined from the boundary conditions, the interface relations Eqs. (9) and (10) and the condition that the displacements and the electric potential are finite at $r = 0$.

5.3 Transverse shear strain

Under this loading mode, displacement boundary conditions at the far field ($r^{ext} \to \infty$) read:

$$
\begin{aligned}
u_r^{ext} &= \gamma r^{ext} \sin 2\theta, \\
u_\theta^{ext} &= \gamma r^{ext} \cos 2\theta, \\
u_z^{ext} &= 0
\end{aligned}
\tag{26}
$$

where γ is an arbitrary known constant. The analytical solution for the displacement field at every r, θ and z takes the form

$$
\begin{aligned}
u_r^{(q)} &= r\sum_{i=1}^{4} \Xi_{q,i} \psi_{q,i} \left[\frac{r}{a}\right]^{\xi_i - 1} \sin 2\theta, \\
u_\theta^{(q)} &= r\sum_{i=1}^{4} \Xi_{q,i} \left[\frac{r}{a}\right]^{\xi_i - 1} \cos 2\theta, \\
u_z^{(q)} &= 0
\end{aligned}
\tag{27}
$$

with

$$
\begin{aligned}
&\xi_1 = 3, && \psi_{q,1} = \frac{k^{(q)} - m^{(q)}}{2k^{(q)} + m^{(q)}} \\
&\xi_2 = 1, && \psi_{q,2} = 1, \\
&\xi_3 = -3, && \psi_{q,3} = -1 \\
&\xi_4 = -1, && \psi_{q,4} = \frac{k^{(q)} + m^{(q)}}{m^{(q)}}
\end{aligned}
\tag{28}
$$

The known coefficients $\Xi_{q,i}$ are determined from the boundary conditions, the interface relations Eqs. (9) and (10) and the condition that the displacements and the electric potential are finite at $r=0$.

5.3 Plane strain/axial electric field

Under this loading mode, displacement and electric potential boundary conditions at the far field ($r^{ext}\to\infty$) read:

$$\begin{aligned} u_r^{ext} &= \beta r^{ext} + \gamma r^{ext}\cos 2\theta, \\ u_\theta^{ext} &= -\gamma r^{ext}\sin 2\theta, \\ u_z^{ext} &= 0, \\ \phi^{ext} &= -\beta^e z \end{aligned} \tag{29}$$

where β, γ and β^e are arbitrary known constants. The analytical solution for the displacement field and the electric potential at every r, θ and z takes the form

$$\begin{aligned} u_r^{(q)} &= r\sum_{i=1}^{4}\Xi_{q,i}\left[\frac{r}{a}\right]^{\xi_i-1}\cos 2\theta + r\sum_{i=1}^{2}Z_{q,i}\left[\frac{r}{a}\right]^{\zeta_i-1}, \\ u_\theta^{(q)} &= -r\sum_{i=1}^{4}\Xi_{q,i}\psi_{q,i}\left[\frac{r}{a}\right]^{\xi_i-1}\sin 2\theta, \\ u_z^{(q)} &= 0, \\ \phi^{(q)} &= -\beta^e z \end{aligned} \tag{30}$$

In the above expressions, $\psi_{q,i}$ and ξ_i for $i=1,2,3,4$ are given by the relations described in the previous boundary value problem. Moreover, $\zeta_1=1$ and $\zeta_2=-1$. The unknown coefficients for the qth phase $\Xi_{q,i}$ and $Z_{q,i}$ are determined from the boundary conditions, the interface relations Eqs. (9) and (10) and the condition that the displacements and the electric potential are finite at $r=0$.

5.5 Hydrostatic strain

For this type of loading, displacement conditions at far field ($r^{ext} \to \infty$, $z^{ext} \to \infty$) correspond to hydrostatic strain:

$$u_r^{ext} = \beta r^{ext}, \quad u_\theta^{ext} = 0, \quad u_z^{ext} = \beta z^{ext} \tag{31}$$

The analytical solution for the displacement field at every r, θ and z takes the form

$$\begin{aligned} u_r^{(q)} &= r\sum_{i=1}^{2} Z_{q,i}\left[\frac{r}{a}\right]^{\zeta_i - 1}, \\ u_\theta^{(q)} &= 0, \\ u_z^{(q)} &= \beta z \end{aligned} \tag{32}$$

with $\zeta_1 = 1$ and $\zeta_2 = -1$. The unknown coefficients $Z_{q,i}$ are determined from the boundary conditions, the interface relations Eqs. (9) and (10) and the condition that the displacements and the electric potential are finite at $r = 0$.

5.6 Computing the dilute concentration tensors

Solving the previously described boundary value problems, the average fields $\mathbf{E}^{(q)}$ can be computed in both the extended fiber (including the interface) and the matrix. In these studies, the constants β, γ and β^e are arbitrary, thus one can choose them properly in order to construct the dilute concentration tensors (for instance, setting one equal to 1 and zeros to the rest). The four discussed boundary value problems are sufficient for identifying $\mathbf{T}$ and $\mathbf{H}$. The computations are included in Appendix B for the reader's convenience. Similar computational procedure is described in Chatzigeorgiou and Meraghni [57]; Chatzigeorgiou et al. [56]; Chen et al.[24] .

6. Numerical Results

In this section, the new Mori-Tanaka scheme considering energetic surfaces is utilized to obtain a full set of homogenized properties of nanoporous composites where the surface piezoelectricity

effect prevails. In the following examples, the matrix phase is considered to be PZT-7A. The piezoelectric properties of the considered materials can be found in Chen et al. [58], which are also listed in Table 1. The surface parameters are typically identified from extensive molecular dynamics simulations of atomic lattices of finite thickness by progressively reducing the number of through-thickness atomic planes and extrapolating the limit to zero [25]. Most publications in the literature used two sets of surface elastic constants, obtained by the molecular dynamics simulations for two different crystallographic orientations [25], which yield stiffening and softening behavior of such materials at the nanoscale with decreasing pore sizes due to the positive and negative surface energy, respectively. Since a full set of surface parameters for PZT-7A are not available in the open literature, the surface parameters are taken as known quantities. As customary, to vigorously test the accuracy of the extended Mori-Tanaka approach, two types of surface parameters labeled as surface A and surface B, listed in Table 2, are considered, which yield negative and positive surface energies respectively. It should be noted that a justification of the applicability of the surface parameters with negative surface energy density remains an open question due to the lack of reliable experimental methods. Nevertheless, they serve as good candidates for critically assessing the predictive capability of the continuum mechanics-based simulation of elastic nanostructured materials with the extended Gurtin-Murdoch interfaces. It is worth mentioning that thermodynamically there is no restriction about the positiveness of the surface properties (contrarily to a bulk material, whose stiffness tensor needs to be positive definite). However, one needs to verify that the chosen surface parameters do not lead to an unstable overall response [31, 59, 60].

Table 1 Material parameters for the bulk PZT-7A ceramics

$k(\mathrm{GPa})$	$l(\mathrm{GPa})$	$n(\mathrm{GPa})$	$p(\mathrm{GPa})$	$m(\mathrm{GPa})$
112.1	74.24	131	25.30	35.9

$e_{31}\left(\mathrm{Cm}^{-2}\right)$	$e_{33}\left(\mathrm{Cm}^{-2}\right)$	$e_{15}\left(\mathrm{Cm}^{-2}\right)$	$\kappa_{11}\left(\mathrm{nCV}^{-1}\mathrm{m}^{-1}\right)$	$\kappa_{33}\left(\mathrm{nCV}^{-1}\mathrm{m}^{-1}\right)$
-2.324	10.9900	9.31	3.984	2.081

Table 2 Material parameters for the energetic surfaces

Type	$L_{11}^{s}\left(\mathrm{Nm}^{-1}\right)$	$L_{13}^{s}\left(\mathrm{Nm}^{-1}\right)$	$L_{33}^{s}\left(\mathrm{Nm}^{-1}\right)$	$L_{44}^{s}\left(\mathrm{Nm}^{-1}\right)$	
Surface A	-14.8	-7.424	-13.1	-2.53	
Surface B	29.6	14.84	26.2	5.06	
Type	$e_{31}^{s}\left(\mathrm{nCm}^{-1}\right)$	$e_{33}^{s}\left(\mathrm{nCm}^{-1}\right)$	$e_{15}^{s}\left(\mathrm{nCm}^{-1}\right)$	$\kappa_{11}^{s}\left(10^{-18}\mathrm{Cm}^{-1}\right)$	$\kappa_{33}^{s}\left(10^{-18}\mathrm{Cm}^{-1}\right)$
Surface A	0.2324	-1.099	-0.931	-0.3984	-0.2081
Surface B	-0.4648	2.198	1.862	0.7968	0.4162

The extended theory is validated by comparison with the results using the CCA/GSCM technique and the finite-element approach developed in our recent work [44]. This validation is performed for nanoporous PZT-7A with different pore radii and pore volume fractions in large parameter space. It should be noted that, while real porous composites were modelled in Chen et al. [44] by excluding directly porosity from the bulk materials, we mimic porosities by assigning the fiber phase with very low moduli.

Figure 4 illustrates the differences of the axisymmetric moduli k^*, l^* and the axial shear and transverse shear moduli p^* and m^* between the CCA/GSCM predictions by Chen et al. [44] vis-à-vis the extended Mori-Tanaka calculations with 30% of pore volume fraction for Types A and B surfaces for pore radii in the range of 0.5-20 nm in 0.5 nm increment. The results have been normalized by their corresponding values in the absence of surface piezoelectric effects. As anticipated from the classical results without piezoelectric effect, the axisymmetric and axial shear moduli predicted by the extended CCA and Mori-Tanaka schemes are indistinguishable over the entire parameter range. In contrast, the transverse shear moduli generated by the GSCM and the extended Mori-Tanaka methods are non-identical, which is a known issue in classical micromechanics techniques. The differences are even greater at the small pore radii due to the

important surface energies. Figures 5-6 show the comparison of the non-zero piezoelectric and dielectric constants generated by the extended CCA and Mori-Tanaka approach. Once again, remarkable agreements are obtained.

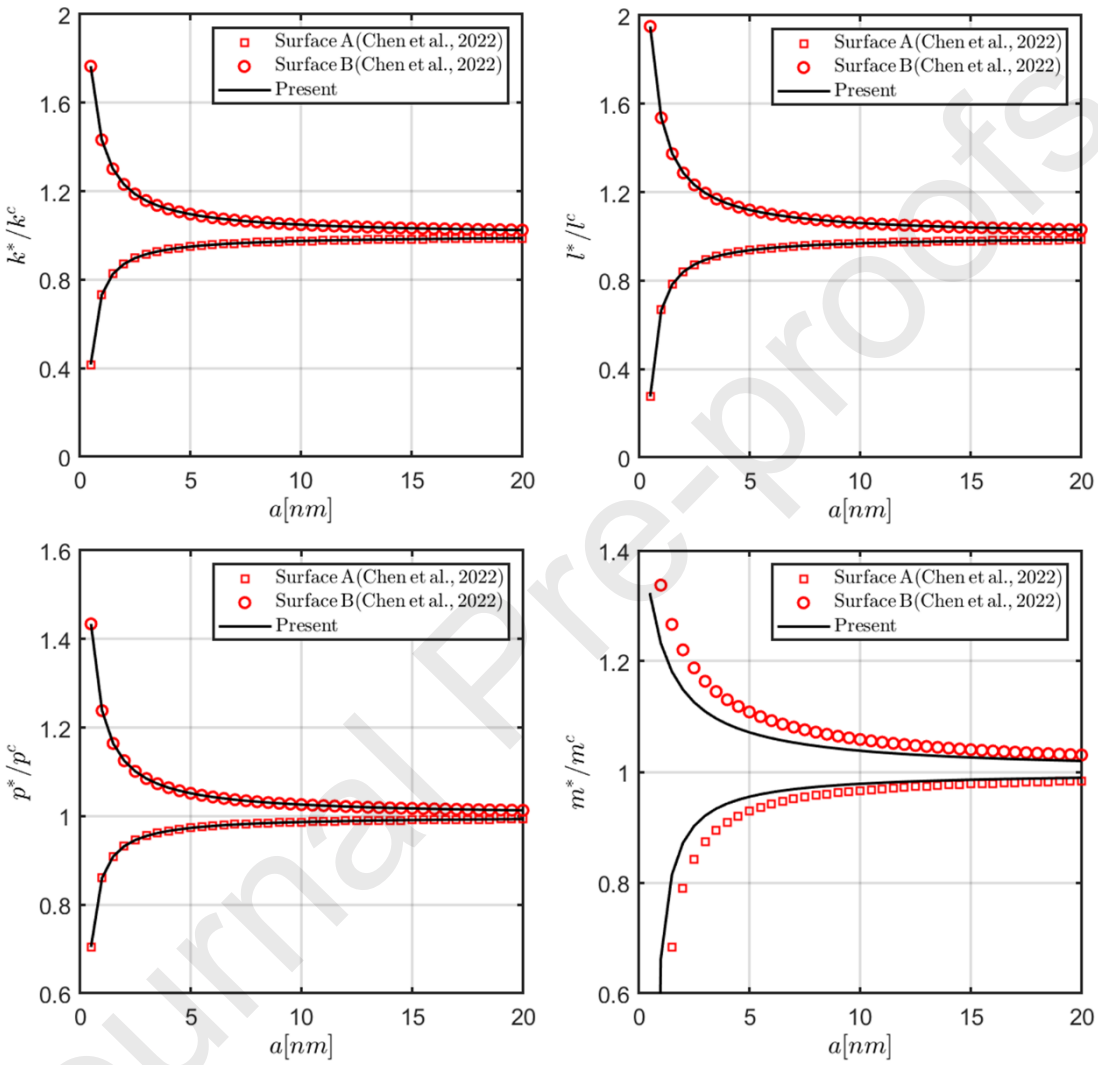

Figure 4 Normalized Hill's axisymmetric and shear moduli of a transversely isotropic porous PZT nanocomposite with 0.30 porosity volume fraction as a function of the porosity radius. Comparison with the CCA and three-phase model predictions of Chen et al. [44]

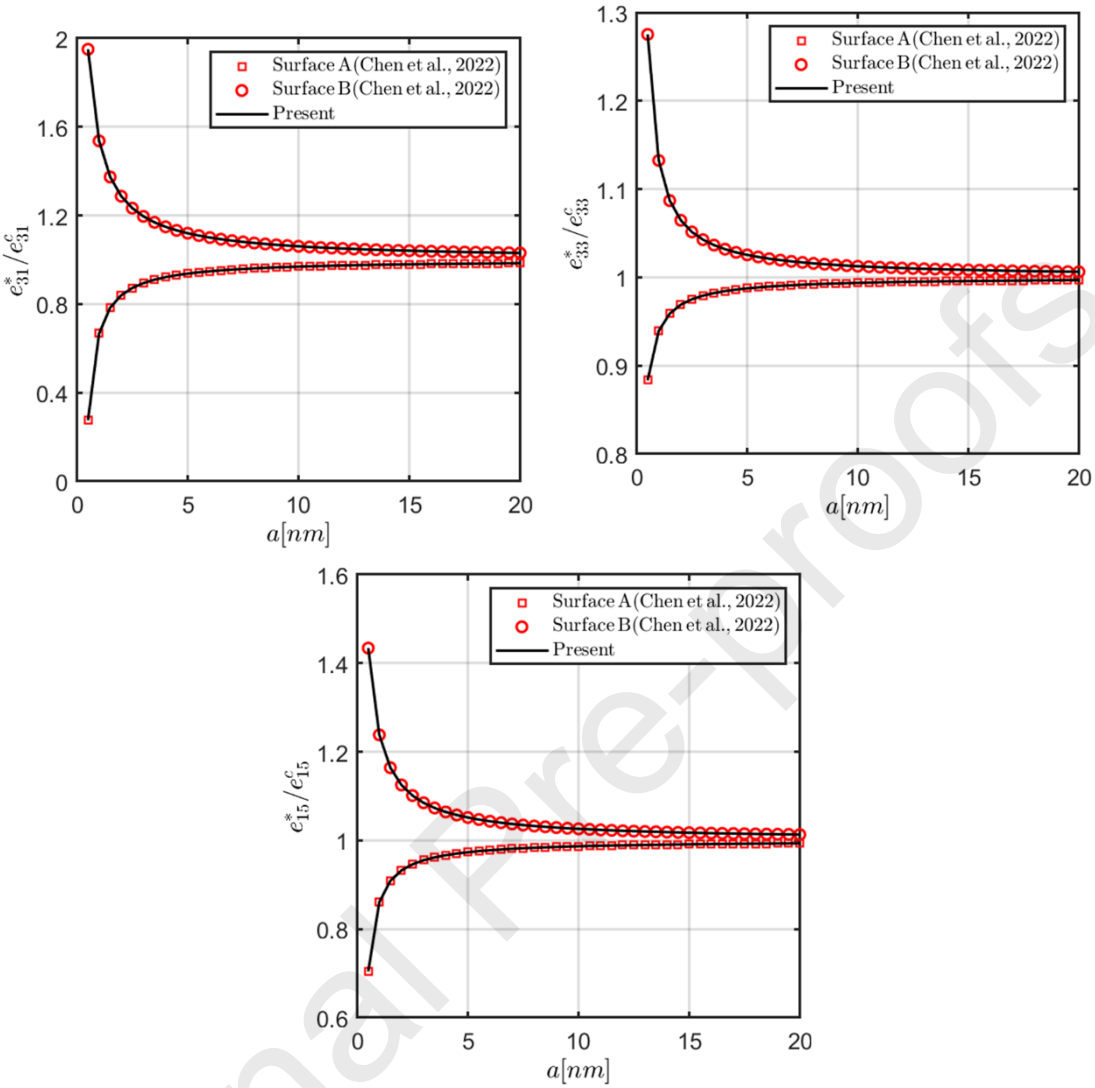

Figure 5 Normalized piezoelectric constants of a transversely isotropic porous PZT nanocomposite with 0.30 porosity volume fraction as a function of the porosity radius. Comparison with the CCA predictions of Chen et al. [44]

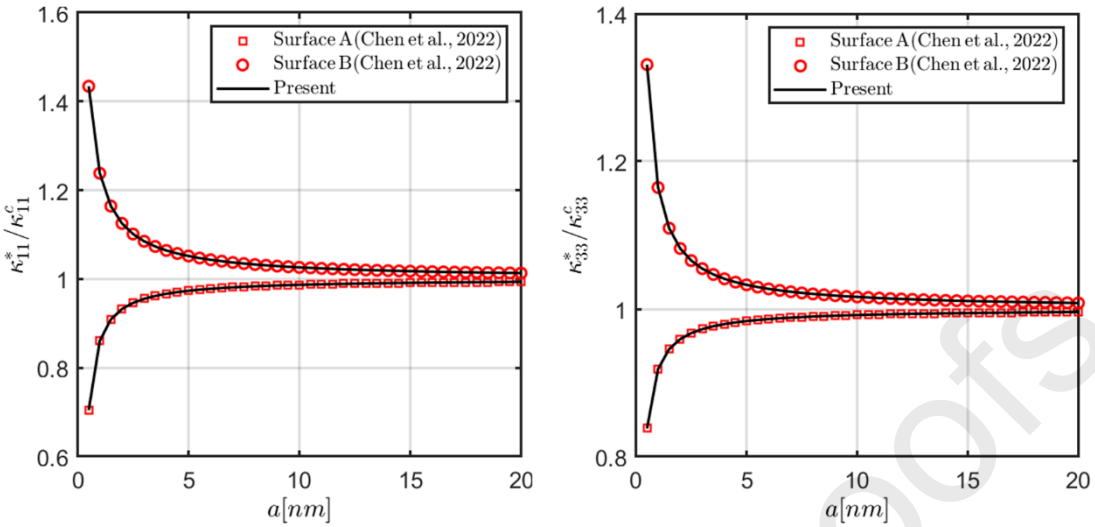

Figure 6 Normalized dielectric constants of a transversely isotropic porous PZT nanocomposite with 0.30 porosity volume fraction as a function of the porosity radius. Comparison with the CCA predictions of Chen et al. [44]

The accuracy of the extended Mori-Tanaka approach to capture the size-dependent multiphysics behavior of nanoporous composites is further demonstrated by comparison with the finite-element results. It should be emphasized that a fundamental difference between the two approaches lies in the fact that while the former provides microstructural detail-free estimates for statistically homogeneous media, the latter explicitly takes into account realistic microstructures under the periodic material assumption. Chen et al. [44] were perhaps the first to investigate in a systematic manner the multiphysics moduli of this class of materials with incorporated surface piezoelectricity using an extended multiphysics finite-element asymptotic homogenization technique. The latter follows the classical homogenization framework described by Cavalcante et al. [61] and Chen and Wang [62]. Namely, the displacement field and electric potential are decomposed into homogenized and fluctuating components considering the scale separation and the unit cell problem is solved using the variational principle, subjected to the periodic boundary condition. In addition, the surface piezoelectricity effect is accounted for through additional surface energies associated with the elements separating different phases. The Mori-Tanaka method with surface piezoelectricity, however, is based on the strong form solution of the interface

equilibrium and electrostatic conditions. Therefore, the solution techniques employed in the extended finite-element and Mori-Tanaka approaches with surface piezoelectricity are totally different, lending to the extended Mori-Tanaka method's rigorous validation.

The unit cell for the finite-element analysis is discretized into 48×12 quadratic quadrilateral elements as shown in Figure 7. The hexagonal repeating unit cell retains the most suitable microstructure for direct comparison with the extended Mori-Tanaka approach as it yields transversely isotropic material properties. The plots of homogenized moduli generated by the finite-element and extended Mori-Tanaka approaches as a function of porosity volume fraction at two different radii a=5nm and a=20nm are presented in Figures 8-10. In the case of transverse shear moduli, the GSCM predictions are also enclosed in the figure for comparison. It is observed the extended Mori-Tanaka and finite-element predictions show remarkable accordance for the axisymmetric and axial shear moduli, piezoelectric and dielectric constants, even at very high-volume fractions. In comparison with the finite element results, the discrepancies of the transverse shear moduli generated by the extended Mori-Tanaka are smaller relative to the GSCM technique.

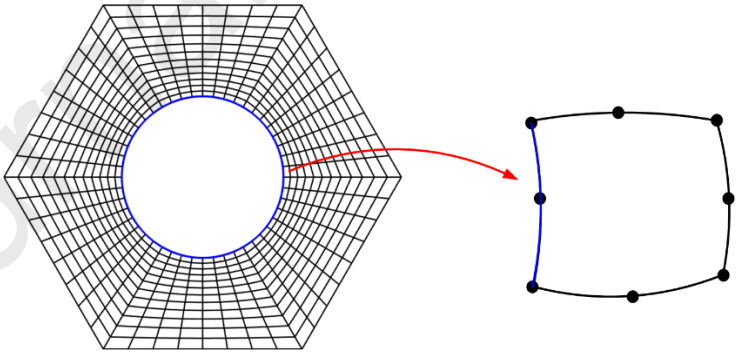

Figure 7 Repeating unit cell discretization using the quadratic quadrilateral element for the finite-element simulation

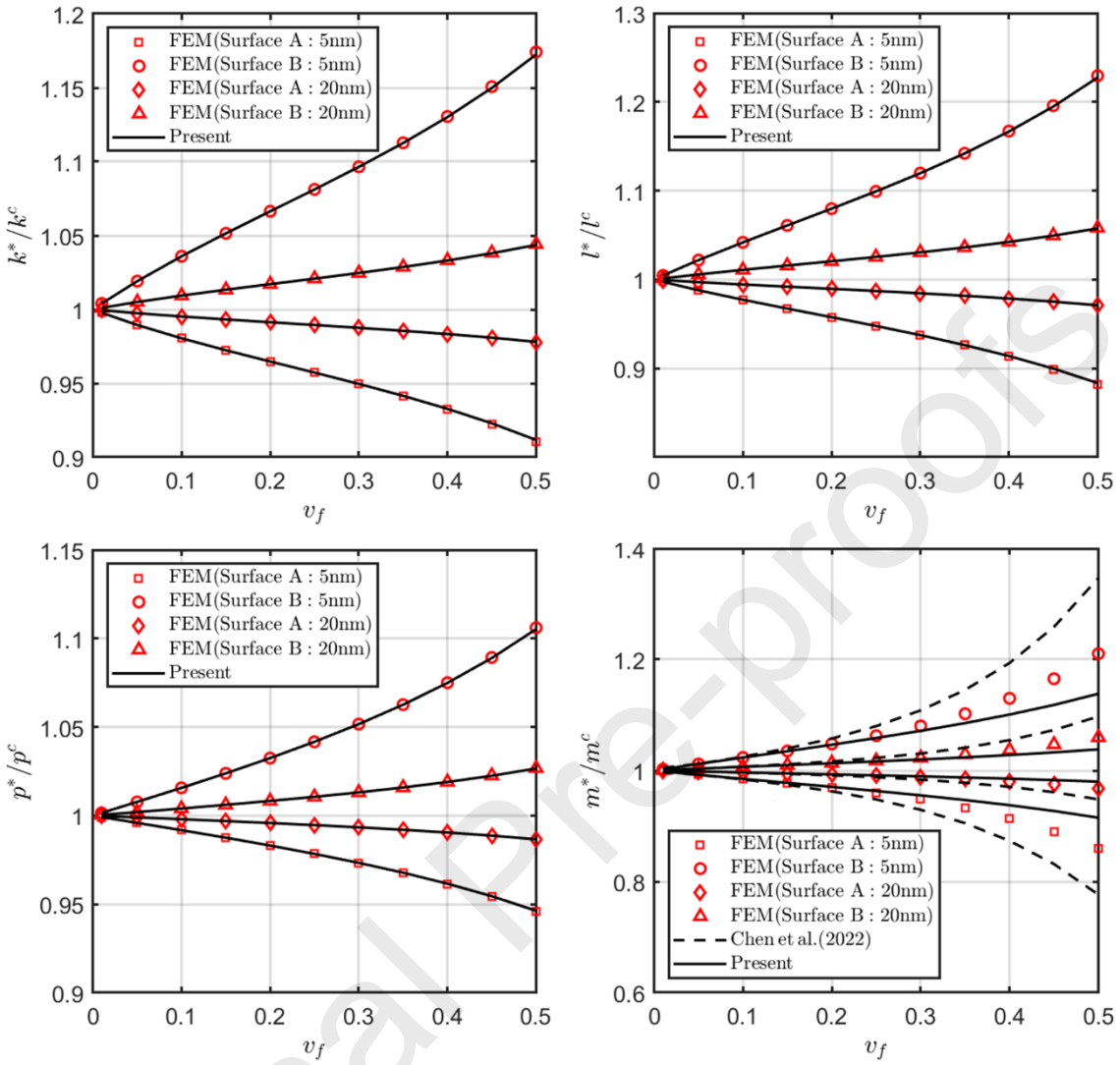

Figure 8 Normalized Hill's axisymmetric and shear moduli of a transversely isotropic porous PZT nanocomposite with 0.30 porosity volume fraction as a function of the porosity radius. Comparison with the finite-element and GSCM predictions of Chen et al. [44]

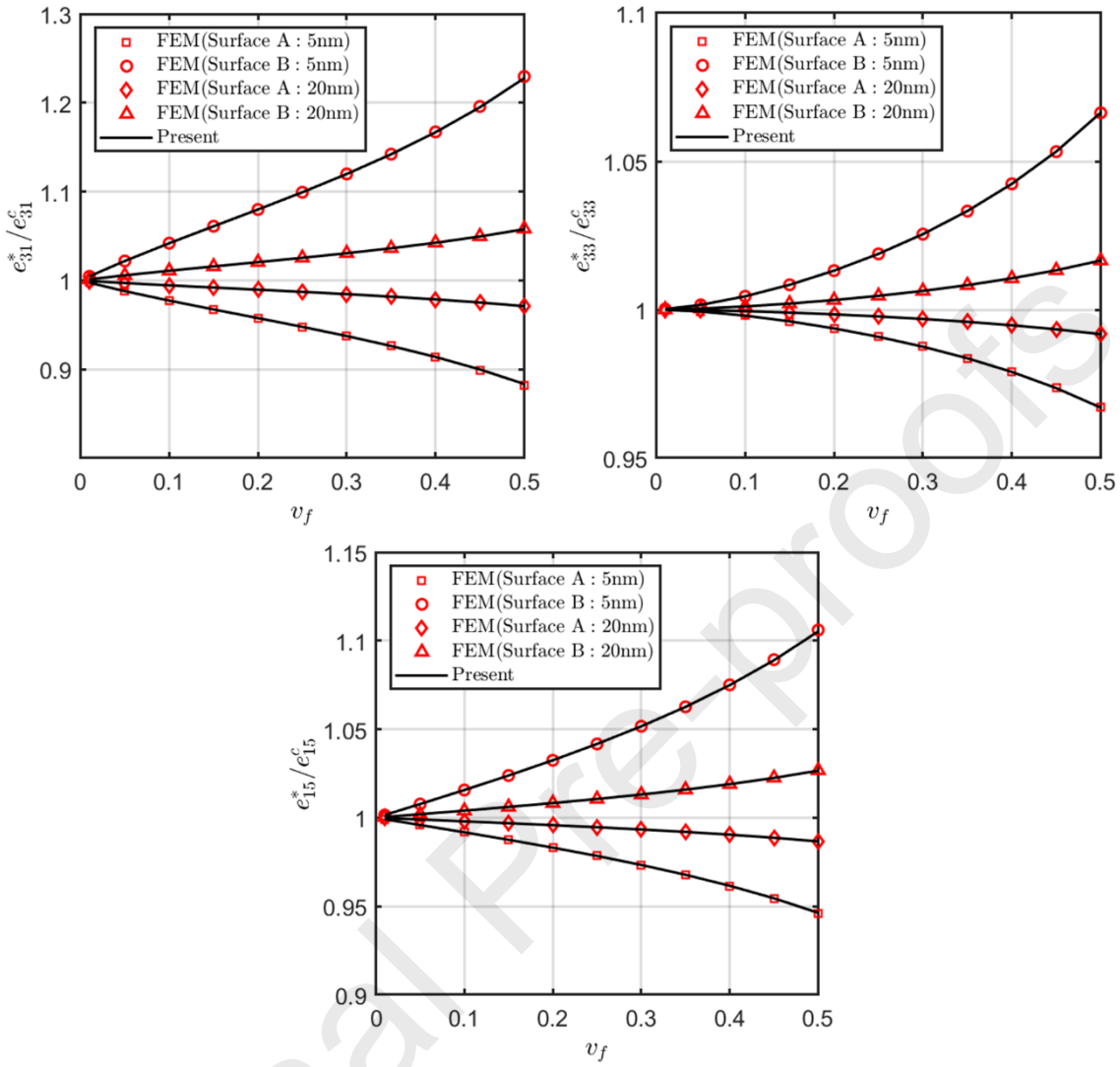

Figure 9 Normalized piezoelectric constants of a transversely isotropic porous PZT nanocomposite with 0.30 porosity volume fraction as a function of the porosity radius. Comparison with the finite-element predictions of Chen et al. [44]

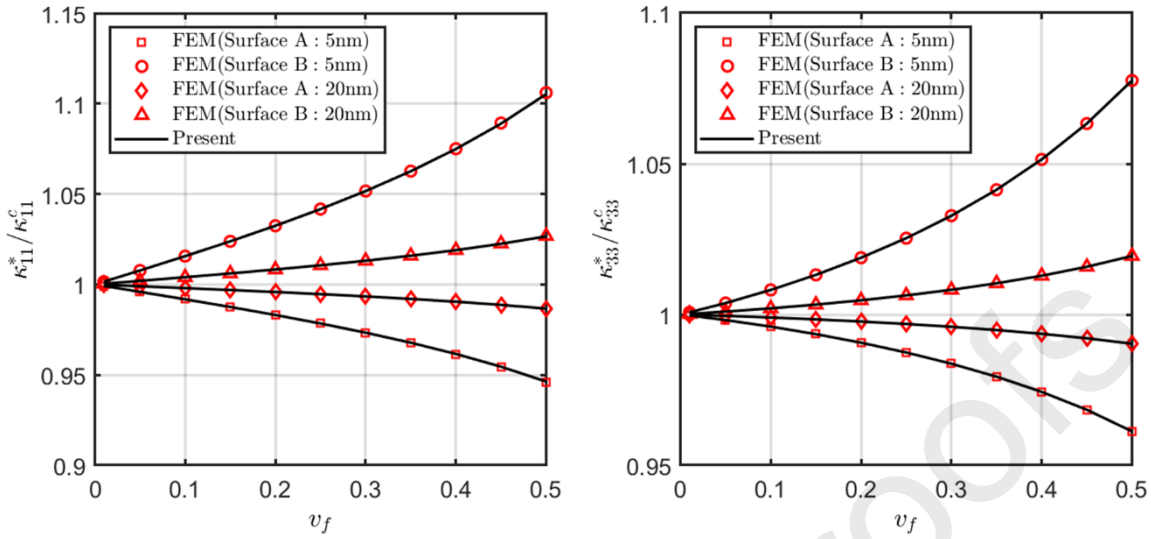

Figure 10 Normalized dielectric constants of a transversely isotropic porous PZT nanocomposite with 0.30 porosity volume fraction as a function of the porosity radius. Comparison with the finite-element predictions of Chen et al. [44]

Piezoelectric ceramics like PZT have very high piezoelectric properties but are difficult to bond onto curved surfaces due to their high stiffness and brittleness. This issue can be circumvented by developing piezoceramic-piezopolymer composites which possess flexibility from the polymer matrix and high piezoelectric properties from piezoelectric ceramics [63]. Therefore, in the last case of the example, we focus on a nanocomposite with unidirectional PZT fiber embedded in a less-active PVDF polymer matrix and study the surface piezoelectricity effect on the effective properties of this material system. The material properties of the PVDF found from [58] were listed in Table 3. The PZT fiber has a fixed volume fraction of 50% but with varying sizes. Figure 11 presents the comparison of the two mechanical constants, n^*, k^*, and two dielectric constants, κ_{11}^* and κ_{33}^*, normalized by their corresponding moduli in the absence of surface piezoelectricity, as a function of the fiber radius, generated by the extended Mori-Tanaka with incorporated Gurtin-Murdoch interface. It is observed that for this materials system, the effective moduli associated with the fiber axial direction (n^* and κ_{33}^*) exhibit remarkable size-

dependent effects for both types of surfaces. However, due to the presence of the soft PVDF matrix, the in-plane moduli (k^* and κ_{11}^*) are less sensitive to the PZT fiber size.

Table 3 Material parameters for the PVDF matrix

$k(\mathrm{GPa})$	$l(\mathrm{GPa})$	$n(\mathrm{GPa})$	$p(\mathrm{GPa})$	$m(\mathrm{GPa})$
3.78	2.22	4.63	0.0526	1.06
$e_{31}\left(\mathrm{Cm}^{-2}\right)$	$e_{33}\left(\mathrm{Cm}^{-2}\right)$	$e_{15}\left(\mathrm{Cm}^{-2}\right)$	$\kappa_{11}\left(\mathrm{nCV}^{-1}\mathrm{m}^{-1}\right)$	$\kappa_{33}\left(\mathrm{nCV}^{-1}\mathrm{m}^{-1}\right)$
0.0043	-0.1099	-0.001999	0.06641	0.07083

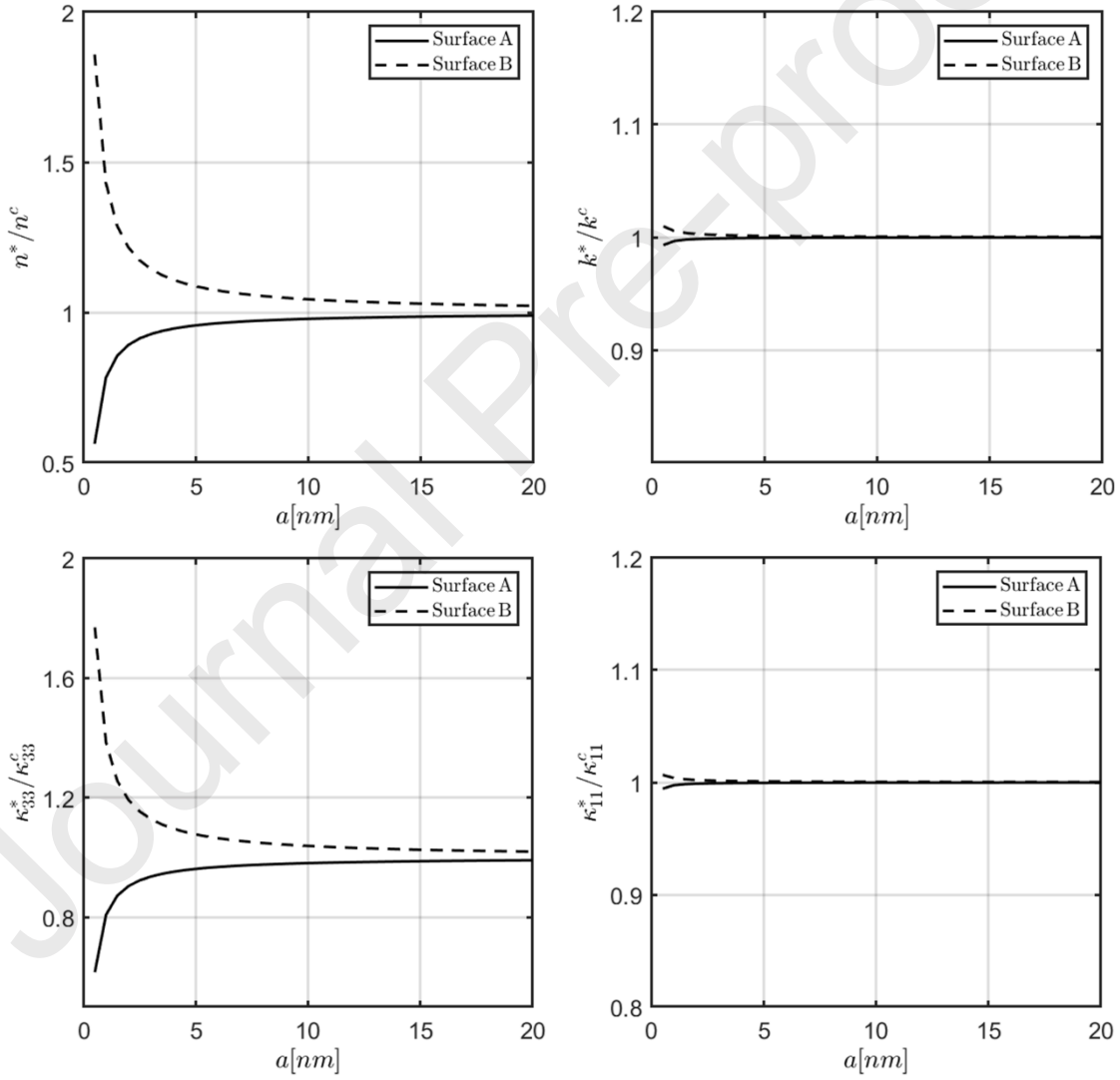

Figure 11 Normalized effective constants of a transversely isotropic PZT/PVDF nanocomposite with 0.50 porosity volume fraction as a function of the fiber radius for two types of surfaces.

7 Conclusion

An extended Mori-Tanaka homogenization approach has been developed for the first time for nanocomposites with transversely isotropic piezoelectric phases by incorporating the surface piezoelectricity effect based on the generalized Gurtin-Murdoch coherent interface model. This extension enables efficient parametric studies of the not-well-characterized unidirectional piezoelectric composites in the nanoparameter range where surface piezoelectric effects have the potential to substantially alter the homogenized moduli under electromechanical loadings.

The main novelty of this work lies in the analytical nature of computing the dilute concentration tenors for both nanofibers and energetic surfaces, derived from the exact solution of Eshleby's inhomogeneity problems under specific macroscopic electromechanical loading conditions. The significant results generated in this work demonstrate that the extended theory is capable of reproducing the size effect of piezoelectric nanocomposites when the characteristic size of the inhomogeneity is sufficiently small. Except for the transverse shear loading, the new mean-field framework yields indistinguishable homogenized moduli relative to the CCA and FE reference results even at high volume fractions and small pore sizes for unidirectional piezoelectric nanocomposites under axisymmetric, axial shear, and electric field loading. The proposed analytical approach not only provides a useful tool for rapid identification of the size-dependent homogenized moduli of nanocomposites under electromechanical loading, but also paves the way for the further extension of the model to account for the inelastic mechanisms through the transformation field analysis technique against which other micromechanics approaches may be compared.

Equation Section 1

Appendix A: Transformation between coordinate systems and useful integrals

The base unit vectors in cylindrical coordinates are written as

$$\mathbf{n}_r = \begin{bmatrix} \cos\theta \\ \sin\theta \\ 0 \end{bmatrix}, \quad \mathbf{n}_\theta = \begin{bmatrix} -\sin\theta \\ \cos\theta \\ 0 \end{bmatrix}, \quad \mathbf{n}_z = \begin{bmatrix} 0 \\ 0 \\ 1 \end{bmatrix} \tag{A34}$$

Transformation between Cartesian and cylindrical coordinate systems for the fields is obtained according to the formulas [64, 65]

$$\begin{aligned} \mathbf{U}^{cyl} &= \mathbf{R} \cdot \mathbf{U}^{Car} \\ \mathbf{E}^{cyl} &= \mathbf{W}_E \cdot \mathbf{E}^{Car} \\ \boldsymbol{\Sigma}^{cyl} &= \mathbf{W}_\Sigma \cdot \boldsymbol{\Sigma}^{Car} \end{aligned} \tag{A35}$$

where

$$\mathbf{R} = \begin{bmatrix} \mathbf{R}_v & \mathbf{0}_{3\times1} \\ \mathbf{0}_{1\times3} & 1 \end{bmatrix}, \quad \mathbf{W}_E = \begin{bmatrix} \mathbf{Q}_\varepsilon & \mathbf{0}_{6\times3} \\ \mathbf{0}_{3\times6} & \mathbf{R}_v \end{bmatrix}, \quad \mathbf{W}_\Sigma = \begin{bmatrix} \mathbf{Q}_\sigma & \mathbf{0}_{6\times3} \\ \mathbf{0}_{3\times6} & \mathbf{R}_v \end{bmatrix}$$

and

$$\mathbf{R}_v = \begin{bmatrix} \cos\theta & \sin\theta & 0 \\ -\sin\theta & \cos\theta & 0 \\ 0 & 0 & 1 \end{bmatrix},$$

$$\mathbf{Q}_\varepsilon = \begin{bmatrix} \cos^2\theta & \sin^2\theta & 0 & \frac{1}{2}\sin 2\theta & 0 & 0 \\ \sin^2\theta & \cos^2\theta & 0 & -\frac{1}{2}\sin 2\theta & 0 & 0 \\ 0 & 0 & 1 & 0 & 0 & 0 \\ -\sin 2\theta & \sin 2\theta & 0 & \cos 2\theta & 0 & 0 \\ 0 & 0 & 0 & 0 & \cos\theta & \sin\theta \\ 0 & 0 & 0 & 0 & -\sin\theta & \cos\theta \end{bmatrix},$$

$$\mathbf{Q}_\sigma = \begin{bmatrix} \cos^2\theta & \sin^2\theta & 0 & \sin 2\theta & 0 & 0 \\ \sin^2\theta & \cos^2\theta & 0 & -\sin 2\theta & 0 & 0 \\ 0 & 0 & 1 & 0 & 0 & 0 \\ -\frac{1}{2}\sin 2\theta & \frac{1}{2}\sin 2\theta & 0 & \cos 2\theta & 0 & 0 \\ 0 & 0 & 0 & 0 & \cos\theta & \sin\theta \\ 0 & 0 & 0 & 0 & -\sin\theta & \cos\theta \end{bmatrix}$$

The average $\mathbf{E}^{(1)}$ in the inhomogeneities/interfaces system is expressed in cylindrical coordinates as

$$\mathbf{E}^{(1)} = \frac{1}{2L\pi a^2}\int_{-L}^{L}\int_0^{2\pi} \boldsymbol{\mathcal{N}}_r^{\mathrm{T}} \cdot \mathbf{U}'\big|_{r=a} a\mathrm{d}\theta\mathrm{d}z + \frac{1}{2L\pi a^2}\int_0^{2\pi}\int_0^{a} \boldsymbol{\mathcal{N}}_z^{\mathrm{T}} \cdot \left(\mathbf{U}'\big|_{z=L} - \mathbf{U}'\big|_{z=-L}\right) \cdot r\mathrm{d}r\mathrm{d}z \quad \text{(A36)}$$

with

$$\mathbf{U}' = \mathbf{R}^{\mathrm{T}} \cdot \begin{bmatrix} u_r \\ u_\theta \\ u_z \\ \phi \end{bmatrix}^{(1)}, \quad \boldsymbol{\mathcal{N}}_r^{\mathrm{T}} = \begin{bmatrix} \cos\theta & 0 & 0 & 0 \\ 0 & \sin\theta & 0 & 0 \\ 0 & 0 & 0 & 0 \\ \sin\theta & \cos\theta & 0 & 0 \\ 0 & 0 & \cos\theta & 0 \\ 0 & 0 & \sin\theta & 0 \\ 0 & 0 & 0 & \cos\theta \\ 0 & 0 & 0 & \sin\theta \\ 0 & 0 & 0 & 0 \end{bmatrix}, \quad \boldsymbol{\mathcal{N}}_z^{\mathrm{T}} = \begin{bmatrix} 0 & 0 & 0 & 0 \\ 0 & 0 & 0 & 0 \\ 0 & 0 & 1 & 0 \\ 0 & 0 & 0 & 0 \\ 1 & 0 & 0 & 0 \\ 0 & 1 & 0 & 0 \\ 0 & 0 & 0 & 0 \\ 0 & 0 & 0 & 0 \\ 0 & 0 & 0 & 1 \end{bmatrix}$$

For the interface, we introduce the extended stress $\boldsymbol{\Sigma}^{(s)}$

$$\boldsymbol{\Sigma}^{(s)} = \left[0, \sigma_{\theta\theta}^{(s)}, \sigma_{zz}^{(s)}, 0, 0, \sigma_{\theta z}^{(s)}, 0, \mathrm{d}l_\theta^{(s)}, \mathrm{d}l_z^{(s)}\right]^{\mathrm{T}} \quad \text{(A37)}$$

Thus the average $\boldsymbol{\Sigma}^{(1)}$ in the inhomogeneities/interfaces system is expressed in cylindrical coordinates as

$$\boldsymbol{\Sigma}^{(1)} = \frac{1}{2L\pi a^2}\int_{-L}^{L}\int_0^{2\pi}\int_0^{a} \mathbf{W}_E^{\mathrm{T}} \cdot \boldsymbol{\Sigma} r\mathrm{d}r\mathrm{d}\theta\mathrm{d}z + \frac{1}{2L\pi a^2}\int_{-L}^{L}\int_0^{2\pi} \mathbf{W}_E^{\mathrm{T}} \cdot \boldsymbol{\Sigma}^{(s)} a\mathrm{d}r\mathrm{d}z \quad \text{(A38)}$$

Equation Section (Next)

Appendix B: Analytical computations for the four boundary value problems

The unknown constants $\Xi_{q,i}$, $\Xi^{e}_{q,i}$ and $Z_{q,i}$ are identified using i) the boundary conditions at $r = r^{ext}$, ii) the consistency condition that the fields should be finite at $r = 0$, and iii) the interface conditions Eqs. (9) and (10) between the material phases.

B.1. Axial shear/in-plane electric field

For this boundary value problem, the boundary conditions and the fact that all fields should be finite at $r = 0$ yield

$$\Xi_{1,2} = \Xi^{e}_{1,2} = 0, \quad \Xi_{0,1} = \beta, \quad \Xi^{e}_{0,1} = \beta^{e} \tag{B40}$$

The rest of the unknown constants are given by the solution of the system

$$\mathbf{K}_{xz} \cdot \boldsymbol{\Xi} = \beta \mathbf{F}_{xz} + \beta^{e} \mathbf{F}^{e}_{xz} \tag{B41}$$

where

$$\boldsymbol{\Xi} = \begin{bmatrix} \Xi_{1,1} \\ \Xi_{0,2} \\ \Xi^{e}_{1,1} \\ \Xi^{e}_{0,2} \end{bmatrix}, \quad \mathbf{F}_{xz} = \begin{bmatrix} 1 \\ p^{(0)} \\ 0 \\ e^{(0)}_{15} \end{bmatrix}, \quad \mathbf{F}^{e}_{xz} = \begin{bmatrix} 1 \\ -e^{(0)}_{15} \\ 0 \\ \kappa^{(0)}_{11} \end{bmatrix},$$

$$\mathbf{K}_{xz} = \begin{bmatrix} 1 & -1 & 0 & 0 \\ p^{(1)} & p^{(0)} & -e^{(1)}_{15} & -e^{(0)}_{15} \\ 0 & 0 & 1 & -1 \\ e^{(1)}_{15} & e^{(0)}_{15} & \kappa^{(1)}_{11} & \kappa^{(0)}_{11} \end{bmatrix} + \frac{1}{a} \begin{bmatrix} 0 & 0 & 0 & 0 \\ L^{(s)}_{66} & 0 & -e^{(s)}_{26} & 0 \\ 0 & 0 & 0 & 0 \\ e^{(s)}_{26} & 0 & \kappa^{(s)}_{22} & 0 \end{bmatrix}$$

The solution of this system can be written in the form

$$\boldsymbol{\Xi} = \beta \boldsymbol{\Xi}^{mec} + \beta^{e} \boldsymbol{\Xi}^{elc} \tag{B42}$$

The average $\mathbf{E}$ and $\boldsymbol{\Sigma}$ in the fiber are given by

$$\mathbf{E}^{(1)}=\begin{bmatrix}0\\0\\0\\0\\\Lambda_{xz}\\0\\\Lambda^{e}_{xz}\\0\\0\end{bmatrix},\qquad \mathbf{\Sigma}^{(1)}=\begin{bmatrix}0\\0\\0\\0\\M_{xz}\\0\\M^{e}_{xz}\\0\\0\end{bmatrix}+\frac{1}{a}\begin{bmatrix}0\\0\\0\\0\\M^{s}_{xz}\\0\\M^{se}_{xz}\\0\\0\end{bmatrix} \tag{B43}$$

with

$$\begin{aligned}
\Lambda_{xz}&=\Xi_{1,1},\\
\Lambda^{e}_{xz}&=-\Xi^{e}_{1,1},\\
M_{xz}&=p^{(1)}\Xi_{1,1}-e^{(1)}_{15}\Xi^{e}_{1,1},\\
M^{e}_{xz}&=e^{(1)}_{15}\Xi_{1,1}+\kappa^{(1)}_{11}\Xi^{e}_{1,1},\\
M^{s}_{xz}&=L^{(s)}_{66}\Xi_{1,1}-e^{(s)}_{26}\Xi^{e}_{1,1},\\
M^{se}_{xz}&=e^{(s)}_{26}\Xi_{1,1}+\kappa^{(s)}_{22}\Xi^{e}_{1,1}
\end{aligned}$$

All the above constants can be written in the form

$$\mathbf{\Phi}=\beta\mathbf{\Phi}^{mec}+\beta^{e}\mathbf{\Phi}^{elc} \tag{B44}$$

with regard to the far-field conditions

$$\mathbf{E}^{(0)}=\left[0,0,0,0,\beta,0,-\beta^{e},0,0\right]^{\mathrm{T}}$$

B.2. Transverse shear

For this boundary value problem, the boundary conditions and the fact that all fields should be finite at $r=0$ yield

$$\Xi_{1,3}=\Xi_{1,4}=\Xi_{0,1}=0,\quad \Xi_{0,2}=\gamma \tag{B45}$$

The rest of the unknown constants are given by the solution of the system

$$\mathbf{K}_{xy}\cdot\mathbf{\Xi}=\gamma\mathbf{F}_{xy} \tag{B46}$$

with

$$\mathbf{\Xi} = \begin{bmatrix} \Xi_{1,1} \\ \Xi_{1,2} \\ \Xi_{0,3} \\ \Xi_{0,4} \end{bmatrix}, \qquad \mathbf{F}_{xy} = \begin{bmatrix} 1 \\ 2m^{(0)} \\ 1 \\ 2m^{(0)} \end{bmatrix}$$

$$\mathbf{K}_{xy} = \begin{bmatrix} \psi_{1,1} & 1 & 1 & -\psi_{0,4} \\ 0 & 2m^{(1)} & -6m^{(0)} & -4k^{(0)} \\ 1 & 1 & -1 & -1 \\ k_{41} & 2m^{(1)} & 6m^{(0)} & -2k^{(0)} \end{bmatrix} + \frac{1}{a}\begin{bmatrix} 0 & 0 & 0 & 0 \\ -\psi^s & -L_{22}^{(s)} & 0 & 0 \\ 0 & 0 & 0 & 0 \\ 2\psi^s & 2L_{22}^{(s)} & 0 & 0 \end{bmatrix}$$

with

$$k_{41} = \frac{6k^{(1)}m^{(1)}}{2k^{(1)} + m^{(1)}}, \qquad \psi^s = \left[2 - \psi_{1,1}\right] L_{22}^{(s)}$$

The solution of this system can be written in the form

$$\mathbf{\Xi} = \gamma \mathbf{\Xi}^{mec} \tag{B47}$$

The average $\mathbf{E}$ and Σ in the fiber are given by

$$\mathbf{E}^{(1)} = 2\begin{bmatrix} 0 \\ 0 \\ 0 \\ \Lambda_{xy} \\ 0 \\ 0 \\ 0 \\ 0 \end{bmatrix}, \qquad \mathbf{\Sigma}^{(1)} = 2\begin{bmatrix} 0 \\ 0 \\ 0 \\ M_{xy} \\ 0 \\ 0 \\ 0 \\ 0 \end{bmatrix} + \frac{2}{a}\begin{bmatrix} 0 \\ 0 \\ 0 \\ M_{xy}^s \\ 0 \\ 0 \\ 0 \\ 0 \end{bmatrix} \tag{B48}$$

with

$$\Lambda_{xy} = \frac{1+\psi_{1,1}}{2}\Xi_{1,1} + \Xi_{1,2},$$
$$M_{xy} = m^{(1)}\Lambda_{xy},$$
$$M^{s}_{xy} = \frac{L^{(s)}_{22}}{4}\left[\left[2-\psi_{1,1}\right]\Xi_{1,1} + \Xi_{1,2}\right]$$

All the above constants can be written in the form

$$\mathbf{\Phi} = \gamma\mathbf{\Phi}^{mec} \tag{B49}$$

with regard to the far-field conditions

$$\mathbf{E}^{(0)} = 2\gamma\left[0,0,0,1,0,0,0,0,0\right]^{\mathrm{T}}$$

B.3. Plane strain/axial electric field

For this boundary value problem, the boundary conditions and the fact that all fields should be finite at $r = 0$ yield

$$\begin{aligned}&\Xi_{1,3} = \Xi_{1,4} = \Xi_{0,1} = Z_{1,2} = 0,\\ &\Xi_{0,2} = \gamma,\\ &Z_{0,1} = \beta\end{aligned} \tag{B50}$$

The rest of the unknown constants are given by the solution of two systems:

1. The first is written as

$$\mathbf{K}_{xx}\cdot\mathbf{Z} = \beta\mathbf{F}_{xx} + \beta^{e}\mathbf{F}^{e}_{xx} \tag{B51}$$

with

$$\mathbf{Z} = \begin{bmatrix} Z_{1,1} \\ Z_{0,2} \end{bmatrix}, \quad \mathbf{F}_{xx} = \begin{bmatrix} 1 \\ 2k^{(0)} \end{bmatrix}, \quad \mathbf{F}^{e}_{xx} = \begin{bmatrix} 0 \\ e^{(1)}_{31} - e^{(0)}_{31} \end{bmatrix} + \frac{1}{a}\begin{bmatrix} 0 \\ e^{(s)}_{32} \end{bmatrix}$$

$$\mathbf{K}_{xx} = \begin{bmatrix} 1 & -1 \\ 2k^{(1)} & 2m^{(0)} \end{bmatrix} + \frac{1}{a}\begin{bmatrix} 0 & 0 \\ L^{(s)}_{22} & 0 \end{bmatrix}$$

The solution is written in the form

$$\mathbf{Z} = \beta\mathbf{Z}^{mec} + \beta^{e}\mathbf{Z}^{elc} \tag{B52}$$

2. The second is written as

$$\mathbf{K}_{xy}\cdot\boldsymbol{\Xi}=\gamma\mathbf{F}_{xy} \tag{B53}$$

where $\boldsymbol{\Xi}$, $\mathbf{F}_{xy}$ and $\mathbf{K}_{xy}$ are given by Eq. (B46).

The average $\mathbf{E}$ and $\boldsymbol{\Sigma}$ in the fiber are given by

$$\mathbf{E}^{(1)}=\begin{bmatrix}\Lambda_{xx}+\Lambda_{xy}\\ \Lambda_{xx}-\Lambda_{xy}\\ 0\\ 0\\ 0\\ 0\\ 0\\ 0\\ -\beta^{e}\end{bmatrix},\qquad \boldsymbol{\Sigma}^{(1)}=\begin{bmatrix}M_{xx}+2M_{xy}-\beta^{e}e_{31}^{(1)}\\ M_{xx}-2M_{xy}-\beta^{e}e_{31}^{(1)}\\ M_{zz}-\beta^{e}e_{33}^{(1)}\\ 0\\ 0\\ 0\\ 0\\ 0\\ M_{xx}^{e}+\beta^{e}\kappa_{33}^{(1)}\end{bmatrix}+\frac{1}{a}\begin{bmatrix}M_{xx}^{s}+2M_{xy}^{s}-\beta^{e}e_{32}^{(s)}\\ M_{xx}^{s}-2M_{xy}^{s}-\beta^{e}e_{32}^{(s)}\\ M_{zz}^{s}-2\beta^{e}e_{33}^{(s)}\\ 0\\ 0\\ 0\\ 0\\ 0\\ M_{xx}^{se}+2\beta^{e}\kappa_{33}^{(s)}\end{bmatrix} \tag{B54}$$

with

$$\begin{aligned}\Lambda_{xx}&=Z_{1,1},\\ M_{xx}&=2k^{(1)}Z_{1,1},\\ M_{zz}&=2l^{(1)}Z_{1,1},\\ M_{xx}^{e}&=2e_{31}^{(1)}Z_{1,1},\\ M_{xx}^{s}&=L_{22}^{(s)}Z_{1,1},\\ M_{zz}^{s}&=2L_{23}^{(s)}Z_{1,1},\\ M_{xx}^{se}&=2e_{32}^{(s)}Z_{1,1}\end{aligned} \tag{B55}$$

The constants Λ_{xy}, M_{xy}, M_{xy}^{s} are the same as those of the expressions in Eq. (B48).

All the above constants can be written in the form

$$\boldsymbol{\Phi}=\beta\boldsymbol{\Phi}^{mec}+\beta^{e}\boldsymbol{\Phi}^{elc} \tag{B56}$$

with regard to the far field

$$\mathbf{E}^{(0)}=\left[\beta+\gamma,\beta-\gamma,0,0,0,0,0,0,-\beta^{e}\right]^{\mathrm{T}} \tag{B57}$$

B.4. Hydrostatic strain

For this boundary value problem, the boundary conditions and the fact that all fields should be finite at $r = 0$ yield

$$Z_{1,2} = 0, \quad Z_{0,1} = \beta \tag{B58}$$

The rest of the unknown constants are given by the solution of the system:

$$\mathbf{K}_{xx} \cdot \mathbf{Z} = \beta \mathbf{F}_h \tag{B59}$$

with

$$\mathbf{Z} = \begin{bmatrix} Z_{1,1} \\ Z_{0,2} \end{bmatrix}, \qquad \mathbf{F}_h = \begin{bmatrix} 1 \\ 2k^{(0)} + l^{(0)} - l^{(1)} \end{bmatrix} + \frac{1}{a} \begin{bmatrix} 0 \\ -L_{23}^{(s)} \end{bmatrix}$$

and $\mathbf{K}_{xx}$ is given by Eq. (B51).

The solution is written in the form

$$\mathbf{Z} = \beta \mathbf{Z}^{mec} \tag{B60}$$

The average $\mathbf{E}$ and Σ in the fiber are given by

$$\mathbf{E}^{(1)} = \begin{bmatrix} \Lambda_h \\ \Lambda_h \\ \beta \\ 0 \\ 0 \\ 0 \\ 0 \\ 0 \\ 0 \end{bmatrix}, \qquad \mathbf{\Sigma}^{(1)} = \begin{bmatrix} M_{xh} \\ M_{xh} \\ M_{zh} \\ 0 \\ 0 \\ 0 \\ 0 \\ 0 \\ M_{xh}^{e} \end{bmatrix} + \frac{1}{a} \begin{bmatrix} M_{xh}^{s} \\ M_{xh}^{s} \\ M_{zh}^{s} \\ 0 \\ 0 \\ 0 \\ 0 \\ 0 \\ M_{xh}^{se} \end{bmatrix} \tag{B61}$$

with

$$
\begin{aligned}
\Lambda_h &= Z_{1,1},\\
M_{xh} &= 2k^{(1)}Z_{1,1} + l^{(1)},\\
M_{zh} &= 2l^{(1)}Z_{1,1} + n^{(1)},\\
M^{e}_{xh} &= e^{(1)}_{31}\left[2Z_{1,1} + 1\right],\\
M^{s}_{xh} &= L^{(s)}_{22}Z_{1,1} + L^{(s)}_{23},\\
M^{s}_{zh} &= 2L^{(s)}_{23}Z_{1,1} + 2L^{(s)}_{33},\\
M^{se}_{xh} &= 2e^{(s)}_{32}Z_{1,1} + 2e^{(s)}_{23}
\end{aligned}
$$

All the above constants can be written in the form

$$\mathbf{\Phi} = \beta\mathbf{\Phi}^{mec} \tag{B62}$$

with regard to the far field

$$\mathbf{E}^{(0)} = \beta\left[1,1,1,0,0,0,0,0,0\right]^{\mathrm{T}}$$

B.5. Summary

From these results, the dilute concentration tensors have the following form

$$
\mathbf{T} = \begin{bmatrix}
T_{11} & T_{12} & T_{13} & 0 & 0 & 0 & 0 & 0 & T_{19}\\
T_{12} & T_{11} & T_{13} & 0 & 0 & 0 & 0 & 0 & T_{19}\\
0 & 0 & 1 & 0 & 0 & 0 & 0 & 0 & 0\\
0 & 0 & 0 & T_{44} & 0 & 0 & 0 & 0 & 0\\
0 & 0 & 0 & 0 & T_{55} & 0 & T_{57} & 0 & 0\\
0 & 0 & 0 & 0 & 0 & T_{55} & 0 & T_{57} & 0\\
0 & 0 & 0 & 0 & T_{75} & 0 & T_{77} & 0 & 0\\
0 & 0 & 0 & 0 & 0 & T_{75} & 0 & T_{77} & 0\\
0 & 0 & 0 & 0 & 0 & 0 & 0 & 0 & 1
\end{bmatrix} \tag{B63}
$$

$$\mathbf{H}=\begin{bmatrix} H_{11} & H_{12} & H_{13} & 0 & 0 & 0 & 0 & 0 & H_{19} \\ H_{12} & H_{11} & H_{13} & 0 & 0 & 0 & 0 & 0 & H_{19} \\ H_{31} & H_{31} & H_{33} & 0 & 0 & 0 & 0 & 0 & H_{39} \\ 0 & 0 & 0 & H_{44} & 0 & 0 & 0 & 0 & 0 \\ 0 & 0 & 0 & 0 & H_{55} & 0 & H_{57} & 0 & 0 \\ 0 & 0 & 0 & 0 & 0 & H_{55} & 0 & H_{57} & 0 \\ 0 & 0 & 0 & 0 & H_{75} & 0 & H_{77} & 0 & 0 \\ 0 & 0 & 0 & 0 & 0 & H_{75} & 0 & H_{77} & 0 \\ H_{91} & H_{91} & H_{93} & 0 & 0 & 0 & 0 & 0 & H_{99} \end{bmatrix} + \frac{1}{a}\begin{bmatrix} H^s_{11} & H^s_{12} & H^s_{13} & 0 & 0 & 0 & 0 & 0 & H^s_{19} \\ H^s_{12} & H^s_{11} & H^s_{13} & 0 & 0 & 0 & 0 & 0 & H^s_{19} \\ H^s_{31} & H^s_{31} & H^s_{33} & 0 & 0 & 0 & 0 & 0 & H^s_{39} \\ 0 & 0 & 0 & H^s_{44} & 0 & 0 & 0 & 0 & 0 \\ 0 & 0 & 0 & 0 & H^s_{55} & 0 & H^s_{57} & 0 & 0 \\ 0 & 0 & 0 & 0 & 0 & H^s_{55} & 0 & H^s_{57} & 0 \\ 0 & 0 & 0 & 0 & H^s_{75} & 0 & H^s_{77} & 0 & 0 \\ 0 & 0 & 0 & 0 & 0 & H^s_{75} & 0 & H^s_{77} & 0 \\ H^s_{91} & H^s_{91} & H^s_{93} & 0 & 0 & 0 & 0 & 0 & H^s_{99} \end{bmatrix} \tag{B64}$$

where the elements of each matrix are obtained by solving the boundary volume problems detailed in Appendices B.1-B.4.

Data Availablity

The raw/processed data required to reproduce these findings cannot be shared at this time as the data also forms part of an ongoing study

References

[1] Barenblatt GI. The formation of equilibrium cracks during brittle fracture. General ideas and hypotheses. Axially-symmetric cracks. Journal of applied mathematics and mechanics. 1959;23:622-36.

[2] Needleman A. A continuum model for void nucleation by inclusion debonding. Journal of Applied Mechanics. 1987;54:525-31.

[3] Tu W, Pindera M-J. Cohesive zone-based damage evolution in periodic materials via finite-volume homogenization. Journal of Applied Mechanics. 2014;81:101005.

[4] Benveniste Y, Miloh T. Imperfect soft and stiff interfaces in two-dimensional elasticity. Mechanics of Materials. 2001;33:309-23.

[5] Hashin Z. Thin interphase/imperfect interface in elasticity with application to coated fiber composites. Journal of the Mechanics and Physics of Solids. 2002;50:2509-37.

[6] Jiang J, Zhao J, Pang S, Meraghni F, Siadat A, Chen Q. Physics-informed deep neural network enabled discovery of size-dependent deformation mechanisms in nanostructures. International Journal of Solids and Structures. 2022;236-237:111320.

[7] Wang X, Zhou K, Wu MS. Interface cracks with surface elasticity in anisotropic bimaterials. International Journal of Solids and Structures. 2015;59:110-20.

[8] Chatzigeorgiou G, Meraghni F, Javili A. Generalized interfacial energy and size effects in composites. Journal of the Mechanics and Physics of Solids. 2017;106:257-82.

[9] Firooz S, Javili A. Understanding the role of general interfaces in the overall behavior of composites and size effects. Computational Materials Science. 2019;162:245-54.

[10] Firooz S, Chatzigeorgiou G, Meraghni F, Javili A. Homogenization accounting for size effects in particulate composites due to general interfaces. Mechanics of Materials. 2019;139:103204.

[11] Benveniste Y. A general interface model for a three-dimensional curved thin anisotropic interphase between two anisotropic media. Journal of the Mechanics and Physics of Solids. 2006;54:708-34.

[12] Tu W, Chen Q. Evolution of interfacial debonding of a unidirectional graphite/polyimide composite under off-axis loading. Engineering Fracture Mechanics. 2020;230:106947.

[13] Buryachenko VA. Local and Nonlocal Micromechanics of Heterogeneous Materials: Springer, 2022.

[14] Gibbs JW. The collected works of J. Willard Gibbs. Yale Univ. Press; 1948.

[15] Javili A, Steinmann P. A finite element framework for continua with boundary energies. Part I: The two-dimensional case. Computer Methods in Applied Mechanics and Engineering. 2009;198:2198-208.

[16] Chen Q, Sun Y, Wang G, Pindera M-J. Finite-volume homogenization and localization of nanoporous materials with cylindrical voids. Part 2: New results. European Journal of Mechanics - A/Solids. 2019;73:331-48.

[17] Chen T, Chiu M-S, Weng C-N. Derivation of the generalized Young-Laplace equation of curved interfaces in nanoscaled solids. Journal of Applied Physics. 2006;100:074308.

[18] Kushch VI, Mogilevskaya SG, Stolarski HK, Crouch SL. Elastic fields and effective moduli of particulate nanocomposites with the Gurtin–Murdoch model of interfaces. International Journal of Solids and Structures. 2013;50:1141-53.

[19] Kushch VI. Atomistic vs. continuum models of nanoporous elastic solid: Stress fields, size-dependent effective stiffness and surface constants. Mechanics of Materials. 2022;166:104223.

[20] Davydov D, Javili A, Steinmann P. On molecular statics and surface-enhanced continuum modeling of nano-structures. Computational Materials Science. 2013;69:510-9.

[21] Gurtin ME, Murdoch AI. A continuum theory of elastic material surfaces. Archive for rational mechanics and analysis. 1975;57:291-323.

[22] Gurtin ME, Murdoch AI. Surface stress in solids. International Journal of Solids and Structures. 1978;14:431-40.

[23] Pindera M-J, Khatam H, Drago AS, Bansal Y. Micromechanics of spatially uniform heterogeneous media: A critical review and emerging approaches. Composites Part B: Engineering. 2009;40:349-78.

[24] Chen Q, Chatzigeorgiou G, Meraghni F. Extended mean-field homogenization of viscoelastic-viscoplastic polymer composites undergoing hybrid progressive degradation induced by interface debonding and matrix ductile damage. International Journal of Solids and Structures. 2021;210-211:1-17.

[25] Miller RE, Shenoy VB. Size-dependent elastic properties of nanosized structural elements. Nanotechnology. 2000;11:139-47.

[26] Duan HL, Karihaloo BL. Thermo-elastic properties of heterogeneous materials with imperfect interfaces: Generalized Levin's formula and Hill's connections. Journal of the Mechanics and Physics of Solids. 2007;55:1036-52.

[27] Duan HL, Wang J, Karihaloo BL, Huang ZP. Nanoporous materials can be made stiffer than non-porous counterparts by surface modification. Acta Materialia. 2006;54:2983-90.

[28] Chen T, Dvorak GJ, Yu CC. Size-dependent elastic properties of unidirectional nano-composites with interface stresses. Acta Mechanica. 2007;188:39-54.

[29] Mogilevskaya SG, Crouch SL, Stolarski HK, Benusiglio A. Equivalent inhomogeneity method for evaluating the effective elastic properties of unidirectional multi-phase composites with surface/interface effects. International Journal of Solids and Structures. 2010;47:407-18.

[30] Wang G, Chen Q, He Z, Pindera M-J. Homogenized moduli and local stress fields of unidirectional nano-composites. Composites Part B: Engineering. 2018;138:265-77.

[31] Javili A, McBride A, Steinmann P, Reddy BD. Relationships between the admissible range of surface material parameters and stability of linearly elastic bodies. Philosophical Magazine. 2012;92:3540-63.

[32] Chen Q, Pindera M-J. Homogenization and localization of elastic-plastic nanoporous materials with Gurtin-Murdoch interfaces: An assessment of computational approaches. International Journal of Plasticity. 2020;124:42-70.

[33] Chen Q, Wang G, Pindera M-J. Homogenization and localization of nanoporous composites-A critical review and new developments. Composites Part B: Engineering. 2018;155:329-68.

[34] Wang J, Huang Z, Duan H, Yu S, Feng X, Wang G, et al. Surface stress effect in mechanics of nanostructured materials. Acta Mechanica Solida Sinica. 2011;24:52-82.

[35] Firooz S, Steinmann P, Javili A. Homogenization of Composites With Extended General Interfaces: Comprehensive Review and Unified Modeling. Applied Mechanics Reviews. 2021;73.

[36] Mogilevskaya SG, Zemlyanova AY, Kushch VI. Fiber- and Particle-Reinforced Composite Materials With the Gurtin–Murdoch and Steigmann–Ogden Surface Energy Endowed Interfaces. Applied Mechanics Reviews. 2021;73.

[37] Yu J, Wen Y, Yang L, Zhao Z, Guo Y, Guo X. Monitoring on triboelectric nanogenerator and deep learning method. Nano Energy. 2022;92:106698.

[38] Yang L, Wang Y, Zhao Z, Guo Y, Chen S, Zhang W, et al. Particle-Laden Droplet-Driven Triboelectric Nanogenerator for Real-Time Sediment Monitoring Using a Deep Learning Method. ACS Applied Materials & Interfaces. 2020;12:38192-201.

[39] Isaeva AN, Topolov VY. Lead-free 0–3-type composites: From piezoelectric sensitivity to modified figures of merit. Journal of Advanced Dielectrics. 2021;11:2150010.

[40] Thakor SG, Rana VA, Vankar HP, Pandit TR. Dielectric spectroscopy and structural characterization of nano-filler-loaded epoxy resin. Journal of Advanced Dielectrics. 2021;11:2150011.

[41] Thabet A, Fouad M. Assessment of dielectric strength and partial discharges patterns in nanocomposites insulation of single-core power cables. Journal of Advanced Dielectrics. 2021;11:2150022.

[42] Hoang M-T, Yvonnet J, Mitrushchenkov A, Chambaud G. First-principles based multiscale model of piezoelectric nanowires with surface effects. Journal of Applied Physics. 2013;113:014309.

[43] Dai S, Gharbi M, Sharma P, Park HS. Surface piezoelectricity: Size effects in nanostructures and the emergence of piezoelectricity in non-piezoelectric materials. Journal of Applied Physics. 2011;110:104305.

[44] Chen Q, Chatzigeorgiou G, Meraghni F, Javili A. Homogenization of size-dependent multiphysics behavior of nanostructured piezoelectric composites with energetic surfaces. European Journal of Mechanics - A/Solids. 2022;96:104731.

[45] Chen T. Exact size-dependent connections between effective moduli of fibrous piezoelectric nanocomposites with interface effects. Acta Mechanica. 2008;196:205-17.

[46] Xiao JH, Xu YL, Zhang FC. Size-dependent effective electroelastic moduli of piezoelectric nanocomposites with interface effect. Acta Mechanica. 2011;222:59.

[47] Gu ST, Qin L. Variational principles and size-dependent bounds for piezoelectric inhomogeneous materials with piezoelectric coherent imperfect interfaces. International Journal of Engineering Science. 2014;78:89-102.

[48] Hill R. Theory of mechanical properties of fiber-strengthened materials: I. elastic behavior. J Mech Phys Solids. 1964;12:199-212.

[49] Eshelby JD. The determination of the elastic field of an ellipsoidal inclusion, and related problems. Proceedings of the royal society of London Series A Mathematical and physical sciences. 1957;241:376-96.

[50] Gu ST, Liu JT, He QC. Size-dependent effective elastic moduli of particulate composites with interfacial displacement and traction discontinuities. International Journal of Solids and Structures. 2014;51:2283-96.

[51] Duan HL, Yi X, Huang ZP, Wang J. A unified scheme for prediction of effective moduli of multiphase composites with interface effects. Part I: Theoretical framework. Mechanics of Materials. 2007;39:81-93.

[52] Böhm HJ. A short introduction to basic aspects of continuum micromechanics. Cdl-fmd Report. 1998;3.

[53] Hashin Z, Rosen BW. The Elastic Moduli of Fiber-Reinforced Materials. Journal of Applied Mechanics. 1964;31:223-32.

[54] Benveniste Y, Dvorak GJ, Chen T. Stress fields in composites with coated inclusions. Mechanics of Materials. 1989;7:305-17.

[55] Wang Z, Oelkers R, Lee K, Fisher F. Annular Coated Inclusion model and applications for polymer nanocomposites–Part II: Cylindrical inclusions. Mechanics of Materials. 2016;101:50-60.

[56] Chatzigeorgiou G, Javili A, Meraghni F. Micromechanical method for effective piezoelectric properties and electromechanical fields in multi-coated long fiber composites. International Journal of Solids and Structures. 2019;159:21-39.

[57] Chatzigeorgiou G, Meraghni F. Elastic and inelastic local strain fields in composites with coated fibers or particles: theory and validation. Mathematics and Mechanics of Solids. 2019;24:2858-94.

[58] Chen Q, Tu W, Liu R, Chen X. Parametric multiphysics finite-volume theory for periodic composites with thermo-electro-elastic phases. Journal of Intelligent Material Systems and Structures. 2018;29:530-52.

[59] Javili A, McBride A, Steinmann P. Thermomechanics of Solids With Lower-Dimensional Energetics: On the Importance of Surface, Interface, and Curve Structures at the Nanoscale. A Unifying Review. Applied Mechanics Reviews. 2013;65.

[60] Wang G, He Z, Chen Q. The surface effects on solid and hollow nanowires under diametral loading. Applied Mathematical Modelling. 2021;96:697-718.

[61] Cavalcante MAA, Khatam H, Pindera M-J. Homogenization of elastic–plastic periodic materials by FVDAM and FEM approaches – An assessment. Composites Part B: Engineering. 2011;42:1713-30.

[62] Chen Q, Wang G. Computationally-efficient homogenization and localization of unidirectional piezoelectric composites with partially cracked interface. Composite Structures. 2020;232:111452.

[63] Jain A, Kumar SJ, Kumar MR, Ganesh AS, Srikanth S. PVDF-PZT Composite Films for Transducer Applications. Mechanics of Advanced Materials and Structures. 2014;21:181-6.

[64] Chatzigeorgiou G, Charalambakis N, Chemisky Y, Meraghni F. 1 - Mathematical Concepts. In: Chatzigeorgiou G, Charalambakis N, Chemisky Y, Meraghni F, editors. Thermomechanical Behavior of Dissipative Composite Materials: Elsevier; 2017. p. 1-36.

[65] Chatzigeorgiou G, Meraghni F, Charalambakis N. Chapter 1 - Tensors. In: Chatzigeorgiou G, Meraghni F, Charalambakis N, editors. Multiscale Modeling Approaches for Composites: Elsevier; 2022. p. 3-27.

AUTHORSHIP STATEMENT Manuscript title:

Extended mean-field homogenization of unidirectional piezoelectric nanocomposites with generalized Gurtin-Murdoch interfaces

Qiang Chen: Writing - Original Draft, Formal Analysis, Investigation, Validation

George Chatzigeorgiou: Writing - Review & Editing, Conceptualization, Project administration

Fodil Meraghni: Conceptualization, Methodology, Writing - Review & Editing, Formal Analysis

Declaration of interests

☒ The authors declare that they have no known competing financial interests or personal relationships that could have appeared to influence the work reported in this paper.

☐ The authors declare the following financial interests/personal relationships which may be considered as potential competing interests: